

Numerical scheme for solving the nonuniformly forced cubic and quintic Swift-Hohenberg equations strictly respecting the Lyapunov functional

D. L. Coelho^{a,*}, E. Vitral^b, J. Pontes^a, N. Mangiavacchi^a

^a*GESAR Group/UERJ - State University of Rio de Janeiro, 20940-903 Rua Fonseca Teles 121, Rio de Janeiro, RJ, Brazil*

^b*Aerospace Engineering and Mechanics Department, University of Minnesota, 107 Akerman Hall, Minneapolis, MN, USA
55455-0153*

Abstract

Computational modeling of pattern formation in nonequilibrium systems is a fundamental tool for studying complex phenomena in biology, chemistry, materials science and engineering. The pursuit for theoretical descriptions of some among those physical problems led to the Swift-Hohenberg equation (SH3) which describes pattern selection in the vicinity of instabilities. A finite differences scheme, known as Stabilizing Correction (Christov & Pontes; 2001 DOI: 10.1016/S0895-7177(01)00151-0), developed to integrate the cubic Swift-Hohenberg equation in two dimensions, is reviewed and extended in the present paper. The original scheme features Generalized Dirichlet boundary conditions (GDBC), forcings with a spatial ramp of the control parameter, strict implementation of the associated Lyapunov functional, and second order representation of all derivatives. We now extend these results by including periodic boundary conditions (PBC), forcings with gaussian distributions of the control parameter and the quintic Swift-Hohenberg (SH35) model. The present scheme also features a strict implementation of the functional for all test cases. A code verification was accomplished, showing unconditional stability, along with second order accuracy in both time and space. Test cases confirmed the monotonic decay of the Lyapunov functional and all numerical experiments exhibit the main physical features: highly nonlinear behaviour, wavelength filter and competition between bulk and boundary effects.

Keywords: Pattern Formation, Nonlinear Systems, Swift-Hohenberg Equation, Finite Difference Methods

1. Introduction

Understanding the selection and orientation mechanisms of the spatial structures, their symmetries and instabilities represent a major theme of theoretical and experimental research in computational modeling of self-organization phenomena. Nowadays, spatiotemporal organization is recognized to be related to several technological problems in physics, chemistry [1], nonlinear optics [2], and materials science [3, 4, 5]. For computational material science and engineering a long-term goal is to apply such modeling and numerical framework to multiple scales and increasingly larger scale systems in order to achieve predictive capabilities [6,

*Corresponding author. Tel.: +55 (21) 2332-4733

Email addresses: coelho.daniel@posgraduacao.uerj.br (D. L. Coelho), danielcoelho.uerj@gmail.com (D. L. Coelho)

7, 8, 9].

The pursuit for theoretical descriptions of some among those physical problems led to the Swift-Hohenberg (SH) equation [10]. It is a widely accepted model for describing pattern formation in many physical systems presenting symmetry breaking instabilities, such as the emergence of convection rolls in a thin layer of fluid heated from below. It first appeared in the framework of Bénard thermal convection between two “infinite” horizontal surfaces with distinct temperatures, where J. Swift and P. Hohenberg [10] performed a reduction of the full dynamics, led by the Boussinesq equations, to the slow modes dynamics. Such reduction was also accomplished for reaction-diffusion systems where a similar model could be derived with an additional quadratic nonlinearity (SH23) [3, 11]. More recently, an extension of the original Swift-Hohenberg equation (SH3) was proposed with the introduction of a destabilizing cubic term and a quintic one. The resulting quintic SH equation (SH35) admits the coexistence of stable uniform and structured solutions, which may coexist and extends the use of the Swift-Hohenberg equation to the study of localized structures [12].

Roughly speaking, the SH equation has three basic pattern-forming mechanisms, related to each term of the equation. The linear term is accompanied by a control parameter (related to temperature in the case of Rayleigh Bénard convection) and will be addressed as a forcing parameter. It represents how far from the onset of the instability the system is. Secondly, the wavelength filter contains all the equation spatial derivatives and tends to lead the pattern to have the chosen critical wavelength. Finally the nonlinear terms play the interaction between the modes involved in the dynamics. In the SH3, the cubic term is responsible for saturating the linear growth. In the SH35, the cubic term is destabilize the dynamics while the quintic one is responsible for the saturation. Some theoretical works explored nonuniform forcings for the case of Rayleigh Bénard convection [13, 14].

The SH model has a potential form such that we can associate its dynamics to a free energy functional, usually called the Lyapunov functional. In the last years, this potential nature has been explored in the materials science framework as a physical feature associated with the system’s free energy and can be related to the description of materials patterning. In this context, the SH model is part of the phase-field theory, which was developed from statistical mechanics principles, and whose goal is to obtain governing equations for microstructure evolution; it connects thus thermodynamic and kinetic properties with microstructure via a mathematical formalism [5, 7, 15, 16]. The phase-field theory is a descendant of the van der Waals, Cahn-Hilliard and Landau type classical field theoretical approaches, originating from a single order parameter gradient theory of Langer [17, 18]. In the phase-field theory, the local state of matter is characterized by an order parameter $\psi(\mathbf{x}, t)$, called the phase-field variable, which monitors the transition between phases of distinct order of property. It can represent the structural order parameter that measures local crystallinity, the composition of a phase, the degree of a molecular ordering, etc. In the case of the phase-field crystal (PFC) approach, a conserved dynamics is assumed for this order parameter. Although this formalism will not be addressed in this paper, it is worth mentioning that many interesting numerical works explored the SH equation in a PFC framework [19, 20, 21].

There are many works presenting fruitful numerical frameworks for the Swift-Hohenberg equation. In the beginning of this endeavor, Greenside & Coughran Jr. (1984)[22] achieved relevant results through a finite differences approach by using a backward Euler time-integration scheme with rigid [23, 24] and periodic boundary conditions (PBC). Those types of boundary conditions were also explored by Manneville (1990)[25] and Cross (1994)[26]. These works considered uniform control parameters. Other authors employed nonuniform distributions (ramps and gaussians) for the control parameter and presented very interesting results as well, displaying rich competition between bulk and boundary effects. A ramped control parameter mostly appears in the context of rigid boundaries [27, 28], which will be addressed here as Generalized Dirichlet boundary conditions (GDBC), following [27, 29, 28].

Spectral methods have become largely used due to their highly spatial accurate solutions [30, 31, 32]. They usually treat the nonlinear terms explicitly in the physical space and therefore are called pseudo-spectral methods. Fully explicit schemes leads to severe stability restrictions on the time step, because of the fourth-order nonlinear partial differential equation originated from the non-conserved dynamics. In the case of the phase-field crystal (PFC) approach (conserved dynamics), one derives a six-order nonlinear partial differential equation, which is even more restrictive for the time step selection. While PFC is not a subject of this work, our proposed scheme can be readily translated into a numerical framework for many PFC problems.

It is also pertinent to point out that operator splitting methods enable parallel code processing implementation, which allows faster simulations. The usage of sparse matrices also plays a huge role in lowering computational cost in the simulations, and therefore it was implemented in the present work.

The present article is a continuation of the work presented by Christov & Pontes (2002)[29] where those authors employed a finite differences scheme originally introduced by Douglas & Rachford in the framework of the temperature equation, for solving the cubic Swift-Hohenberg equation (SH3) in two dimensions, with uniform forcing, GDBC, and strict implementation of the associated functional. The scheme is known as Stabilizing Correction [33, 34]. Here, we expand this study for additional nonlinearities, boundary conditions and a spatially dependent control parameter. This includes the quintic version of the Swift-Hohenberg equation (SH5) with both GDBC and PBC, nonuniform gaussian distributions of the control parameter in addition to ramps, and also a strict implementation of the associated Lyapunov functional. The scheme features a semi-implicit time splitting with second order representation of time and space derivatives. Some other works also used stabilizing correction scheme for similar fourth-order nonlinear differential equations, such as the anisotropic damped Kuramoto-Sivashinsky equation [35].

A code verification is performed to confirm the unconditional stability of the scheme, along with its second order convergence in both time and space. Since nonlinear partial differential equations do not easily have analytical solutions, which is the SH equation case, the adopted method to verify the order of accuracy of the code is the method of manufactured solutions (MMS). It provides a convenient way of verifying the implementation of nonlinear numerical algorithms, since we can use an artificial (manufactured) solution for

this purpose [36, 37, 35].

This paper is organized as follows. Section 2 briefly discusses the properties of the SH equation and the numerical scheme for solving the cubic and quintic versions of the equation with GDBC and PBC, nonuniform forcings, and the discrete implementation of the associated Lyapunov functional. Section 3 contains all verification procedures adopted. Section 4 presents the numerical experiments. The results are grouped in three parts; the first one showing the steady state patterns obtained in ten simulations with the SH3 equation; the second one showing six simulations with the SH35 and the last one with discussions. Section 5 contains the final remarks of the work.

2. Mathematical modelling and numerical scheme

The mathematical description of the dimensionless governing equations is briefly discussed in the beginning of this section. Then, the details of the numerical framework are exposed as an extension of Christov & Pontes (2002)[29] work. For both SH3 and SH35 discretizations, a finite difference semi-implicit scheme of second order accuracy in time and space is presented. Finally, the choices for the operator splitting method, spatial discretizations and mesh types are clarified.

2.1. Governing equations

The SH equation has the so-called gradient dynamics, which means there is a potential function of the order parameter $\psi(\mathbf{x}, t)$, (known as a Lyapunov functional), that has the property of decreasing monotonically during the evolution [29]. This dynamic equation can be derived from the L^2 -gradient flow of the Lyapunov energy functional:

$$\mathcal{F}[\psi] := \int_{\Omega} d\mathbf{x} \frac{1}{2} \left\{ -\epsilon(\mathbf{x})\psi^2 + \alpha [(q_0^2 + \nabla^2)\psi]^2 - \frac{\beta}{2}\psi^4 + \frac{\gamma}{3}\psi^6 \right\}; \quad (1)$$

$$\frac{\partial \mathcal{F}[\psi]}{\partial t} = - \int_{\Omega} d\mathbf{x} \left(\frac{\partial \psi}{\partial t} \right)^2 \leq 0. \quad (2)$$

where Ω represents the domain whose size is commensurate with the length scales of the patterns. We consider a regular domain $\Omega : \{x \in [0, L_x], y \in [0, L_y]\}$. Also, Eq. 2 denotes the nonincreasing behavior of the Lyapunov functional, which monotonically decreases until steady state is reached [29]. By taking the variational derivative of Eq. 1 in L^2 norm, the following Swift-Hohenberg equation is obtained:

$$\frac{\partial \psi}{\partial t} = - \frac{\delta \mathcal{F}[\psi]}{\delta \psi} = \epsilon(\mathbf{x})\psi - \alpha (q_0^2 + \nabla^2)^2 \psi + \beta \psi^3 - \gamma \psi^5. \quad (3)$$

As discussed by Christov *et al.* [29, 27], the appropriate boundary conditions for this system should consider only production and dissipation in the bulk and not on the boundary ($\partial\Omega$). This can be achieved by assuming Generalized Dirichlet boundary conditions (GDBC), $v = \partial v / \partial n = 0$, where n stands for the outward normal direction to the boundary. Periodic boundary conditions (PBC) will also be addressed in this work, since the absence of boundaries also leads boundary ($\partial\Omega$) integrals to vanish.

We expand Eq. 3 by considering the following laplacian operator in cartesian coordinates: $\nabla^2 \equiv \partial^2/\partial x^2 + \partial^2/\partial y^2$, we have:

$$\begin{aligned}\frac{\partial \psi}{\partial t} &= \epsilon(\mathbf{x})\psi - \alpha q_0^4 \psi - 2\alpha q_0^2 \nabla^2 \psi - \alpha \nabla^4 \psi + \beta \psi^3 - \gamma \psi^5 \\ &= \epsilon(\mathbf{x})\psi - \alpha q_0^4 \psi - 2\alpha q_0^2 \frac{\partial^2 \psi}{\partial x^2} - 2\alpha q_0^2 \frac{\partial^2 \psi}{\partial y^2} - \alpha \frac{\partial^4 \psi}{\partial x^4} - 2\alpha \frac{\partial^4 \psi}{\partial x^2 \partial y^2} - \alpha \frac{\partial^4 \psi}{\partial y^4} + \beta \psi^3 - \gamma \psi^5.\end{aligned}\quad (4)$$

Table 1: Parameters assumed for the governing equations studied in this work.

Equation	Nonlinearity	α	β	γ	q_0
SH3	cubic	1.0	-1.0	0.0	1.0
SH35	quintic	1.0	1.0	1.0	1.0

By using the parameters and values of Tab. 1 in Eq. 3, we define the forms of the SH3 and SH35. The discretization of these governing equations is described in the following subsection.

2.2. The target scheme

In order to construct a Crank-Nicolson second order in time numerical scheme, we adopt the following representation proposed by Christov and Pontes (2002) [29] for the time derivative of Eq. 3, where the RHS is evaluated at the middle of the time step Δt . The updated scheme, now including a quintic term takes the form:

$$\begin{aligned}\frac{\psi^{n+1} - \psi^n}{\Delta t} &= \left[\epsilon(\mathbf{x}) - \alpha q_0^4 - 2\alpha q_0^2 \frac{\partial^2}{\partial x^2} - 2\alpha q_0^2 \frac{\partial^2}{\partial y^2} - \alpha \frac{\partial^4}{\partial x^4} - 2\alpha \frac{\partial^4}{\partial x^2 \partial y^2} - \alpha \frac{\partial^4}{\partial y^4} \right. \\ &\quad \left. + \beta \frac{(\psi^{n+1})^2 + (\psi^n)^2}{2} - \gamma \frac{(\psi^{n+1})^4 + (\psi^n)^4}{2} \right] \left(\frac{\psi^{n+1} + \psi^n}{2} \right).\end{aligned}\quad (5)$$

The superscript $(n+1)$ refers to the next time to be evaluated and n , to the current one. The parameter values for α , β , γ and q_0 are chosen according to Tab. 1.

The RHS terms of Eq. 5 are grouped in three parts, the first and the second ones containing the semi-implicit operators $\Lambda_x^{n+1/2}$ and $\Lambda_y^{n+1/2}$ that will act on the variable $(\psi^{n+1} + \psi^n)/2$, and a function $f^{n+1/2}$, evaluated at the middle of the time step Δt . This function will contain explicit terms only, in the final discrete form of Eq. 5. Space derivatives are represented by centered second order formulæ. Implicit terms are chosen having in mind to construct negative definite operators that will assure the stability of the scheme. The factor $1/2$ multiplying $(\psi^{n+1} + \psi^n)$ in the RHS of the above equation is included in the operators $\Lambda_x^{n+1/2}$ and $\Lambda_y^{n+1/2}$, leading to the following target scheme:

$$\frac{\psi^{n+1} - \psi^n}{\Delta t} = \left(\Lambda_x^{n+1/2} + \Lambda_y^{n+1/2} \right) (\psi^{n+1} + \psi^n) + f^{n+1/2}.\quad (6)$$

For the SH3 equation, the operators $\Lambda_x^{n+1/2}$, $\Lambda_y^{n+1/2}$ and $f^{n+1/2}$ are defined as:

$$\begin{aligned}\Lambda_x^{n+1/2} &= \frac{1}{2} \left[-\alpha \left(\frac{\partial^4}{\partial x^4} + \frac{q_0^4}{2} \right) - \beta \frac{(\psi^{n+1})^2 + (\psi^n)^2}{2} \right]; \\ \Lambda_y^{n+1/2} &= \frac{1}{2} \left[-\alpha \left(\frac{\partial^4}{\partial y^4} + \frac{q_0^4}{2} \right) - \beta \frac{(\psi^{n+1})^2 + (\psi^n)^2}{2} \right]; \\ f^{n+1/2} &= \frac{1}{2} \left[\epsilon(\mathbf{x}) - \alpha \left(2q_0^2 \frac{\partial^2}{\partial x^2} + 2q_0^2 \frac{\partial^2}{\partial y^2} + 2 \frac{\partial^4}{\partial x^2 \partial y^2} \right) \right] (\psi^{n+1} + \psi^n),\end{aligned}\tag{7}$$

and for the SH35:

$$\begin{aligned}\Lambda_x^{n+1/2} &= \frac{1}{2} \left[-\alpha \left(\frac{\partial^4}{\partial x^4} + \frac{q_0^4}{2} \right) - \gamma \frac{(\psi^{n+1})^4 + (\psi^n)^4}{2} \right]; \\ \Lambda_y^{n+1/2} &= \frac{1}{2} \left[-\alpha \left(\frac{\partial^4}{\partial y^4} + \frac{q_0^4}{2} \right) - \gamma \frac{(\psi^{n+1})^4 + (\psi^n)^4}{2} \right]; \\ f^{n+1/2} &= \frac{1}{2} \left[\epsilon(\mathbf{x}) - \alpha \left(2q_0^2 \frac{\partial^2}{\partial x^2} + 2q_0^2 \frac{\partial^2}{\partial y^2} + 2 \frac{\partial^4}{\partial x^2 \partial y^2} \right) \right. \\ &\quad \left. + \beta \frac{(\psi^{n+1})^2 + (\psi^n)^2}{2} \right] (\psi^{n+1} + \psi^n).\end{aligned}\tag{8}$$

2.3. Internal iterations

Since the operators $\Lambda_x^{n+1/2}$, $\Lambda_y^{n+1/2}$ and the function $f^{n+1/2}$ in Eqs. 6, 7 and 8 contain implicit terms due to the time discretization and linearization of the nonlinear terms, we do internal iterations. They are required to secure the approximation of the nonlinearities in the scheme (Eq. 6) at each time step. The iterations loop proceeds until convergence is attained by monitoring the L_∞ norm. The internal iterations scheme reads:

$$\frac{\psi^{n+1,p+1} - \psi^n}{\Delta t} = \left(\Lambda_x^{n+1/2,p} + \Lambda_y^{n+1/2,p} \right) (\psi^{n+1,p+1} + \psi^n) + f^{n+1/2,p},\tag{9}$$

where the index (p) refers to the internal iteration number. The superscript $(n+1, p+1)$ identifies the new iteration, while (n) are the values of the previous time step. The superscript $(n+1)$ for the nonlinear term in the function $f^{n+1/2}$ will be replaced by (n, p) , which stands for the values obtained from the previous iteration.

The operators $\Lambda_x^{n+1/2,p}$, $\Lambda_y^{n+1/2,p}$ function $f^{n+1/2,p}$ are redefined as follows, for the SH3 equation:

$$\begin{aligned}\Lambda_x^{n+1/2,p} &= \frac{1}{2} \left[-\alpha \left(\frac{\partial^4}{\partial x^4} + \frac{q_0^4}{2} \right) - \beta \frac{(\psi^{n+1,p})^2 + (\psi^n)^2}{2} \right], \\ \Lambda_y^{n+1/2,p} &= \frac{1}{2} \left[-\alpha \left(\frac{\partial^4}{\partial y^4} + \frac{q_0^4}{2} \right) - \beta \frac{(\psi^{n+1,p})^2 + (\psi^n)^2}{2} \right], \\ f^{n+1/2,p} &= \frac{1}{2} \left[\epsilon(\mathbf{x}) - \alpha \left(2q_0^2 \frac{\partial^2}{\partial x^2} + 2q_0^2 \frac{\partial^2}{\partial y^2} + 2 \frac{\partial^4}{\partial x^2 \partial y^2} \right) \right] (\psi^{n+1,p} + \psi^n),\end{aligned}\tag{10}$$

and for the SH35:

$$\begin{aligned}
\Lambda_x^{n+1/2,p} &= \frac{1}{2} \left[-\alpha \left(\frac{\partial^4}{\partial x^4} + \frac{q_0^4}{2} \right) - \gamma \frac{(\psi^{n+1,p})^4 + (\psi^n)^4}{2} \right], \\
\Lambda_y^{n+1/2,p} &= \frac{1}{2} \left[-\alpha \left(\frac{\partial^4}{\partial y^4} + \frac{q_0^4}{2} \right) - \gamma \frac{(\psi^{n+1,p})^4 + (\psi^n)^4}{2} \right], \\
f^{n+1/2,p} &= \frac{1}{2} \left[\epsilon(\mathbf{x}) - \alpha \left(2q_0^2 \frac{\partial^2}{\partial x^2} + 2q_0^2 \frac{\partial^2}{\partial y^2} + 2 \frac{\partial^4}{\partial x^2 \partial y^2} \right) \right. \\
&\quad \left. + \beta \frac{(\psi^{n+1,p})^2 + (\psi^n)^2}{2} \right] (\psi^{n+1,p} + \psi^n). \tag{11}
\end{aligned}$$

The iterations proceed until the following criterion for the L_∞ norm is satisfied with $\delta = 1.0 \times 10^{-8}$:

$$L_\infty = \frac{\max |\psi^{n+1,p+1} - \psi^{n+1,p}|}{\max |\psi^{n+1,p+1}|} \leq \delta; \tag{12}$$

so that the last iteration gives the sought function ψ in the new time $\psi^{n+1} \equiv \psi^{n+1,p+1}$.

2.4. The splitting scheme

Although employing sparse matrices for the operators, computationally solving Eq. 9 still represents a costly procedure. In order to reduce such computational effort and errors (from discretization and floating-point operations), the operators splitting method was adopted. The splitting of Eq. 6 is made according to the Douglas second scheme (also known as scheme of stabilizing correction, shown by [27],[29]), and is briefly reviewed. The following equations represent a consistent approximation of the original scheme:

$$\frac{\tilde{\psi} - \psi^n}{\Delta t} = \Lambda_x^{n+1/2,p} \tilde{\psi} + \Lambda_y^{n+1/2,p} \psi^n + f^{n+1/2,p} + (\Lambda_x^{n+1/2,p} + \Lambda_y^{n+1/2,p}) \psi^n, \tag{13}$$

$$\frac{\psi^{n+1,p+1} - \tilde{\psi}}{\Delta t} = \Lambda_y^{n+1/2,p} (\psi^{n+1,p+1} - \psi^n), \tag{14}$$

where $\tilde{\psi}$ is an intermediary estimation of ψ at the new time step. In order to show that the splitting represents the original scheme, we rewrite Eqs. 13 and 14 in the form:

$$(E - \Delta t \Lambda_x^{n+1/2,p}) \tilde{\psi} = (E + \Delta t \Lambda_x^{n+1/2,p}) \psi^n + 2\Delta t \Lambda_y^{n+1/2,p} \psi^n + \Delta t f^{n+1/2,p}, \tag{15}$$

$$(E - \Delta t \Lambda_y^{n+1/2,p}) \psi^{n+1,p+1} = \tilde{\psi} - \Delta t \Lambda_y^{n+1/2,p} \psi^n, \tag{16}$$

where E is the unity operator. Rearranging these equations, the intermediate variable $\tilde{\psi}$ is eliminated and the result may be rewritten as:

$$\begin{aligned}
(E - \Delta t \Lambda_x^{n+1/2,p}) (E - \Delta t \Lambda_y^{n+1/2,p}) \psi^{n+1,p+1} &= (E + \Delta t \Lambda_x^{n+1/2,p}) \psi^n + 2\Delta t \Lambda_y^{n+1/2,p} \psi^n + \\
&\quad + \Delta t f^{n+1/2,p} - (E - \Delta t \Lambda_x^{n+1/2,p}) \Delta t \Lambda_y^{n+1/2,p} \psi^n. \tag{17}
\end{aligned}$$

This result may be rewritten as:

$$\left(E + \Delta t^2 \Lambda_x^{n+1/2,p} \Lambda_y^{n+1/2,p}\right) \frac{\psi^{n+1,p+1} - \psi^n}{\Delta t} = (\Lambda_x^{n+1/2,p} + \Lambda_y^{n+1/2,p})(\psi^{n+1,p+1} + \psi^n) + f^{n+1/2,p}, \quad (18)$$

where E is the unity operator. A comparison with Eq. 6 shows that Eq. 18 is actually equivalent to the former except by the positive definite operator having a norm greater than one:

$$B \equiv E + \Delta t^2 \Lambda_x^{n+1/2,p} \Lambda_y^{n+1/2,p} = E + O(\Delta t^2), \quad (19)$$

which acts on the term $(\psi^{n+1,p+1} - \psi^n)/\Delta t$. This means that this operator does not change the steady state solution. Furthermore, since $\|B\| > 1$, the scheme given by Eqs. 15, and 16 is more stable than the target one (Eq. 6).

2.5. Spatial discretization and boundary conditions

We solve numerically the SH equation with GDBC and PBC. For the case of rigid boundary conditions we adopt a staggered grid, as illustrated in Fig. 1. Consider a staggered mesh in both spatial directions, namely

$$x_i = -\frac{\Delta x}{2} + i \Delta x, \quad \Delta x \equiv \frac{L_x}{n_x - 2}, \quad y_j = -\frac{\Delta y}{2} + j \Delta y, \quad \Delta y \equiv \frac{L_y}{n_y - 2},$$

where n_x and n_y are the number of points in x - and y -directions, respectively. The mesh pattern is shown in Fig. 1. Let $\psi_{i,j}$ be an arbitrary set function defined on the above described mesh. We confine ourselves to the case of constant coefficients. The PBC, which is less restrictive than the GDBC, borrows the crystallography concept of unit cell, which is a repeating pattern representative of the material. That is, using PBC we have a domain that would also act as a unit cell for a infinite two-dimensional surface, with cells being periodically repeated all around the bidimensional domain.

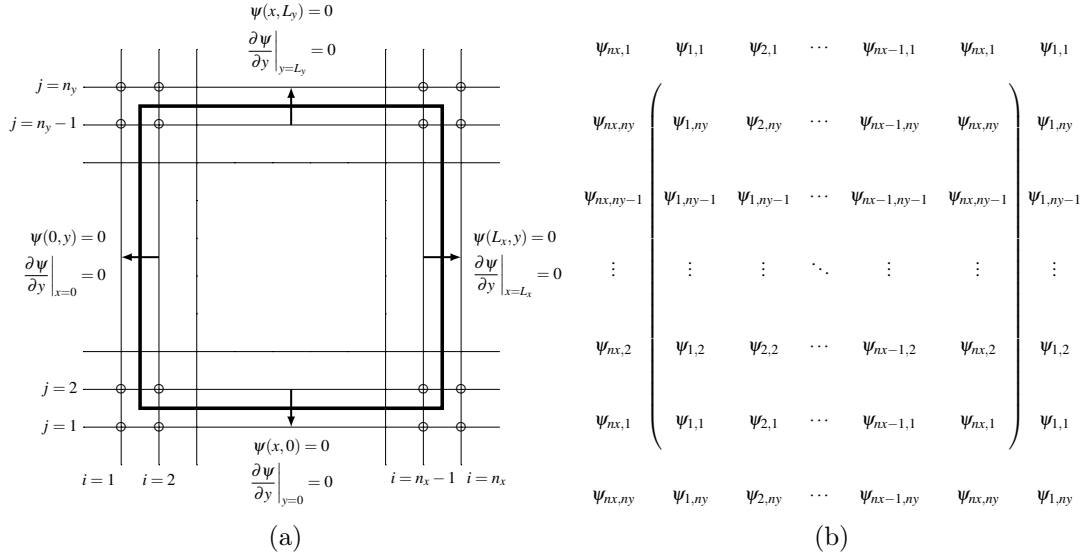


Figure 1: The grids and boundary conditions used in this work. (a) The “Staggered” grid. In the case of GDBC, values of ψ in the first two lines and in the two last ones, and also in the first two columns and in the last two ones are assigned to zero. (b) The periodic domain.

Then the simplest second order symmetric difference approximations of the differential operators are obtained by making a Taylor development of a function ψ at the points of a uniform grid. Considering the function ψ in a bidimensional domain, we can define the derivatives by truncating the Taylor expansion and arranging the equations.

Second derivatives with second order accuracy can be written as:

$$\frac{\partial^2 \psi_{i,j}}{\partial x^2} = \frac{\psi_{i,j-1} - 2\psi_{i,j} + \psi_{i,j+1}}{\Delta x^2}, \quad \frac{\partial^2 \psi_{i,j}}{\partial y^2} = \frac{\psi_{i-1,j} - 2\psi_{i,j} + \psi_{i+1,j}}{\Delta y^2}. \quad (20)$$

And fourth derivatives with second order accuracy are written as:

$$\begin{aligned} \frac{\partial^4 \psi_{i,j}}{\partial x^4} &= \frac{\psi_{i-2,j} - 4\psi_{i-1,j} + 6\psi_{i,j} - 4\psi_{i+1,j} + \psi_{i+2,j}}{\Delta x^4}, \\ \frac{\partial^4 \psi_{i,j}}{\partial y^4} &= \frac{\psi_{i,j-2} - 4\psi_{i,j-1} + 6\psi_{i,j} - 4\psi_{i,j+1} + \psi_{i,j+2}}{\Delta y^4}, \\ \frac{\partial^4 \psi_{i,j}}{\partial x^2 \partial y^2} &= \frac{1}{\Delta x^2 \Delta y^2} \left(\psi_{i-1,j-1} - 2\psi_{i,j-1} + \psi_{i+1,j-1} - 2\psi_{i-1,j} + 4\psi_{i,j} - 2\psi_{i+1,j} + \right. \\ &\quad \left. + \psi_{i-1,j+1} - 2\psi_{i,j+1} + \psi_{i+1,j+1} \right). \end{aligned}$$

Standard second order representations of spatial derivatives are adopted in uniform and structured grids. In order to verify the correctness of the implementation, we conducted convergence tests using the method of manufactured solutions (MMS). The results can be found in Sec. 3.

3. Code verification

One important issue concerning the simulations is the time and mesh size selection, such that we seek reasonable choices inside the stable region of the proposed numerical scheme. The governing equation 3 can be rewritten in the form $P\psi(\mathbf{x}, t) = 0$, where P is an operator containing all the partial derivatives and terms acting on the order parameter $\psi(\mathbf{x}, t)$. The consistency of the numerical scheme can be easily verified since $P\psi(\mathbf{x}, t) - P_{\Delta t, \Delta x, \Delta y}\psi(\mathbf{x}, t) \rightarrow 0$ as $\Delta t, \Delta x, \Delta y \rightarrow 0$, where $P_{\Delta t, \Delta x, \Delta y}$ is the finite difference discretization of P . In this section, scheme stability, free energy functional decay and convergence tests were performed to verify the code implementation.

3.1. Scheme stability

Here, following Christov and Pontes (2001)[29], we study the effect of the time step in the structure evolution by assessing the rate of change in time of the pattern during the simulation. We do this by monitoring \dot{L}_1 , the relative norm rate of change defined as:

$$\dot{L}_1 = \frac{1}{\Delta t} \left(\frac{\sum_{i=1}^{n_x} \sum_{j=1}^{n_y} |\psi_{i,j}^{n+1} - \psi_{i,j}^n|}{\sum_{i=1}^{n_x} \sum_{j=1}^{n_y} |\psi_{i,j}^{n+1}|} \right), \quad (21)$$

which roughly corresponds to the ratio between the spatial average of the modulus of time derivative $\partial\psi/\partial t$ and the spatial average of the modulus of the function itself. The calculations begin from a random initial condition and proceeded until $\dot{L}_1 \leq 5 \times 10^{-7}$, which is our criterion for reaching the steady state. Following this implementation, Fig. 2 shows the system state at $t = 100$ and the steady state attained in six simulations run with different time steps Δt . Fig. 3 shows the evolution of the associated \dot{L}_1 and the curves of the accomplished internal iterations at each time step. This group of simulations was run with GDBC.

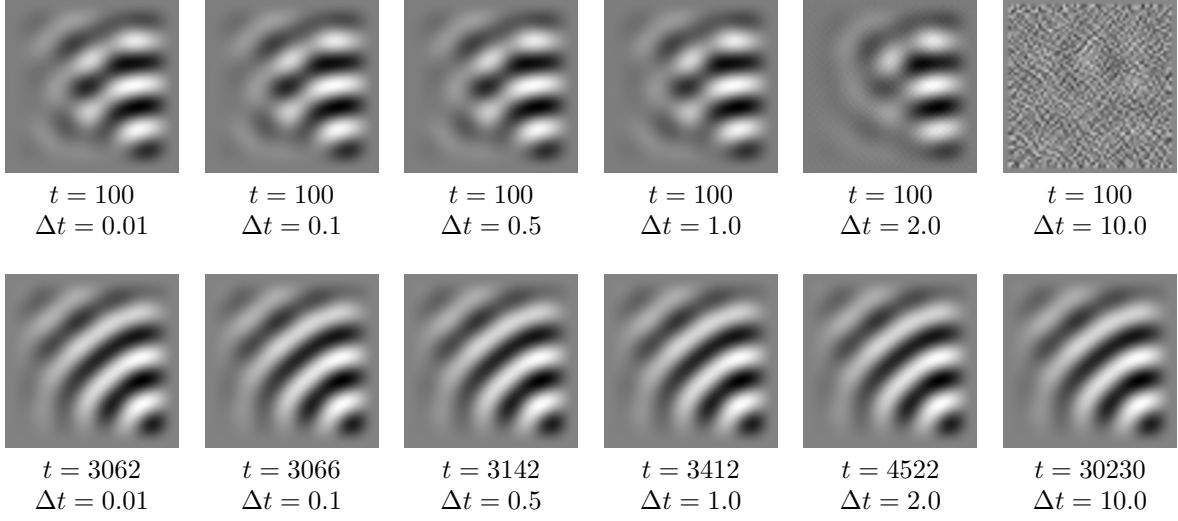


Figure 2: Pattern developed with the SH3 model, GDBC, forced with a spatial ramp of the control parameter given by $0.0 \leq \epsilon(\mathbf{x}) \leq 0.2$, and six different time steps. Top row: transient states at $t = 100$. Bottom: the steady state for the six time steps. All tests started from the exactly same initial condition (pseudo-randomly generated) for a 64×64 nodes domain. Note that the use of larger time steps results in smaller number of required steps to attain the same “time” ($t = 100$ for instance). Errors with larger time steps result in delay in the emergence of the pattern and thus later steady states is expected.

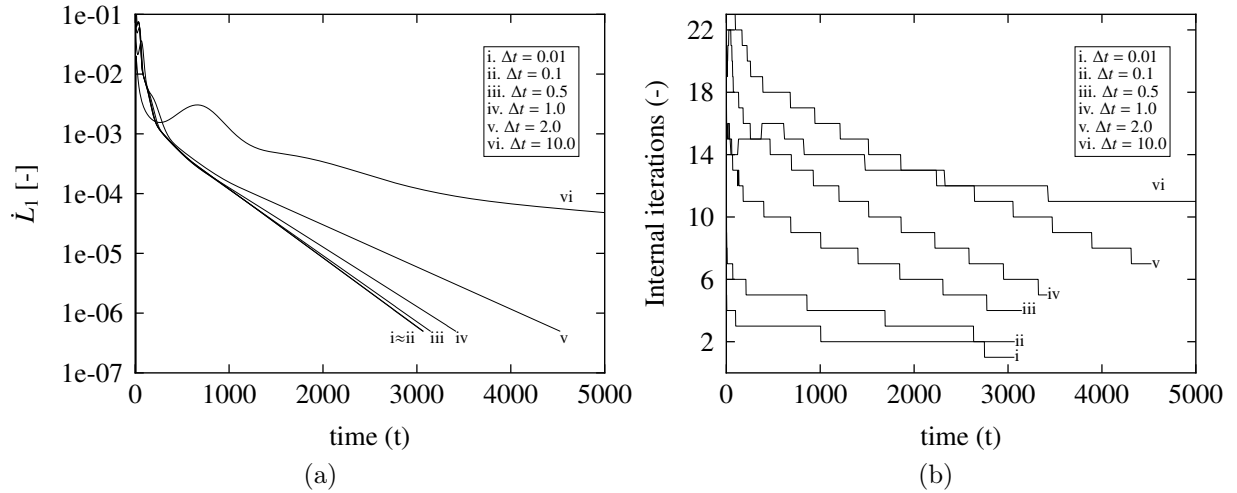


Figure 3: Scheme stability analysis from the numerical integration of the Swift-Hohenberg equation. (a) \dot{L}_1 and (b) internal iterations are shown as a function of time t for a 64×64 nodes domain for all six tests are presented in Fig. 2. The same steady pattern is reached for all six analyzed cases independently of the time step. The simulations started from the same random initial conditions.

Since the semi-implicit scheme is unconditionally stable for any time step, the CPU time to reaching the desired numerical solutions can be optimized without major restrictions to selected time step, as shown by Tab. 2. A conservative choice for all simulations would be $\Delta t = 0.1$, which presents the same \dot{L}_1 decay curve as for $\Delta t = 0.01$. The choice for the remainder of this work was $\Delta t = 0.5$ for the SH3 simulations and $\Delta t = 0.1$ for the SH35, so that lower computational time is required without losing physically consistent transient results given the numerical scheme stability.

Table 2: Computational time spent on each of the simulations presented in 2. simulations.

Time step	Minimum iterations	Maximum iterations	Steady state	Computational time spent
$\Delta t = 0.01$	1	23	$t = 3062$	03 weeks
$\Delta t = 0.1$	2	15	$t = 3066$	14:05:01.20
$\Delta t = 0.5$	4	18	$t = 3142$	03:43:42.92
$\Delta t = 1.0$	5	22	$t = 3412$	03:00:55.56
$\Delta t = 2.0$	7	23	$t = 4522$	02:33:38.59
$\Delta t = 10.0$	7	16	$t = 30230$	02:09:45.01

3.2. Convergence analysis

The adopted method to verify the order of accuracy of the code is the method of manufactured solutions (MMS). It provides a convenient way of verifying the implementation of nonlinear numerical algorithms by using a manufactured (artificial) solution for such purpose [36, 37, 35]. In terms of the proposed problem, we take all the members of the SH equation 3 and consider the following differential equation:

$$F(\psi) = 0, \quad (22)$$

where ψ is the order parameter function that satisfies Eq. 22 and therefore is the PDE solution. The MMS consists of adopting an arbitrary function to be the manufactured solution, $\psi_m(\mathbf{x}, t)$, and since this function is not likely to solve the PDE, a source term is expected, s_m . This term can be seen as an additional forcing function, leading to a modified operator with this new source:

$$\bar{F}(\psi) \equiv F(\psi) - s_m. \quad (23)$$

For the previous equation, $\bar{F}(\psi_m) = 0$ and $\bar{F}(\psi) = -s_m$. Following this new approach to the problem, we find an approximate numerical solution, ψ_k , for the discretized problem so that $\bar{F}(\psi_k) = 0$ or $F(\psi_k) = s_m$. This source term is a minimal intrusion to the code's formulation. The chosen function is periodic with a wavenumber q_1 and is defined as:

$$\psi_m(\mathbf{x}, t) = \psi_0 + \psi_{xy} \cos[q_1(x + y)]e^{at}, \quad (24)$$

where all parameters employed in the manufactured solution and in the differential equation are present on Tab. 3.

Table 3: Parameters assumed for the manufactured solution adopted in the convergence analysis.

MS Parameters	Value	SH Parameters	Value
q_1	$0.25\sqrt{2}q_0$	ϵ	-0.1
q_1^*	$\sqrt{2}q_0$	q_0	1.0
ψ_0	0.0	α	1.0
ψ_{xy}	$\sqrt{ \epsilon }$	β	-1.0
a	0.0	γ	0.0

The global discretization error was examined by the L_2 norm, defined as follows:

$$L_2 = \left(\frac{\sum_{i=1}^{n_x} \sum_{j=1}^{n_y} |(\psi_k)_{i,j}^n - (\psi_m)_{i,j}^n|^2}{\sum_{i=1}^{n_x} \sum_{j=1}^{n_y} |(\psi_m)_{i,j}^n|^2} \right)^{1/2}. \quad (25)$$

In the previous section, a second-order scheme was presented and therefore the formal order of accuracy is two. The observed order of accuracy of the code can be acquired from the global discretization error for meshes with different grid spacing, and can be described by the following relation:

$$p = \frac{\ln(L_2^B/L_2^A)}{\ln(r)}, \quad (26)$$

where L_2^A and L_2^B are the L_2 norm for meshes A and B respectively, and r is the ratio of the grid resolution, g_r , given in number of mesh nodes per critical wavelength of mesh B to A. The meshes employed for the present tests, the number of nodes, and grid resolutions are shown in Tab. 4, and the L_2 curves for the numerical experiments can be seen in Fig. 4.

Table 4: Meshes employed for the code verification by MMS. The chosen domain for the test has 4×4 critical wavelengths. The observed order of accuracy of the code in Fig. 4 can be calculated using Eq. (26) for two cases: $q_1 = 0.25\sqrt{2}q_0$ and $q_1^* = \sqrt{2}q_0$. In the first case the formal order of accuracy is achieved, $p \approx 2.0$, while in the second case $p^* \approx 4.0$ due to discretization error canceling.

Mesh	Number of nodes	Grid resolution (g_r)	Convergence rate (p)	
			($q_1 = 0.25\sqrt{2}q_0$)	($q_1^* = \sqrt{2}q_0$)
Mesh A	16×16	4	-	-
Mesh B	32×32	8	1.99514004	3.95294357
Mesh C	64×64	16	1.99862314	3.98876043
Mesh D	128×128	32	1.99964767	3.99722721
Mesh E	256×256	64	1.99991139	3.99916624

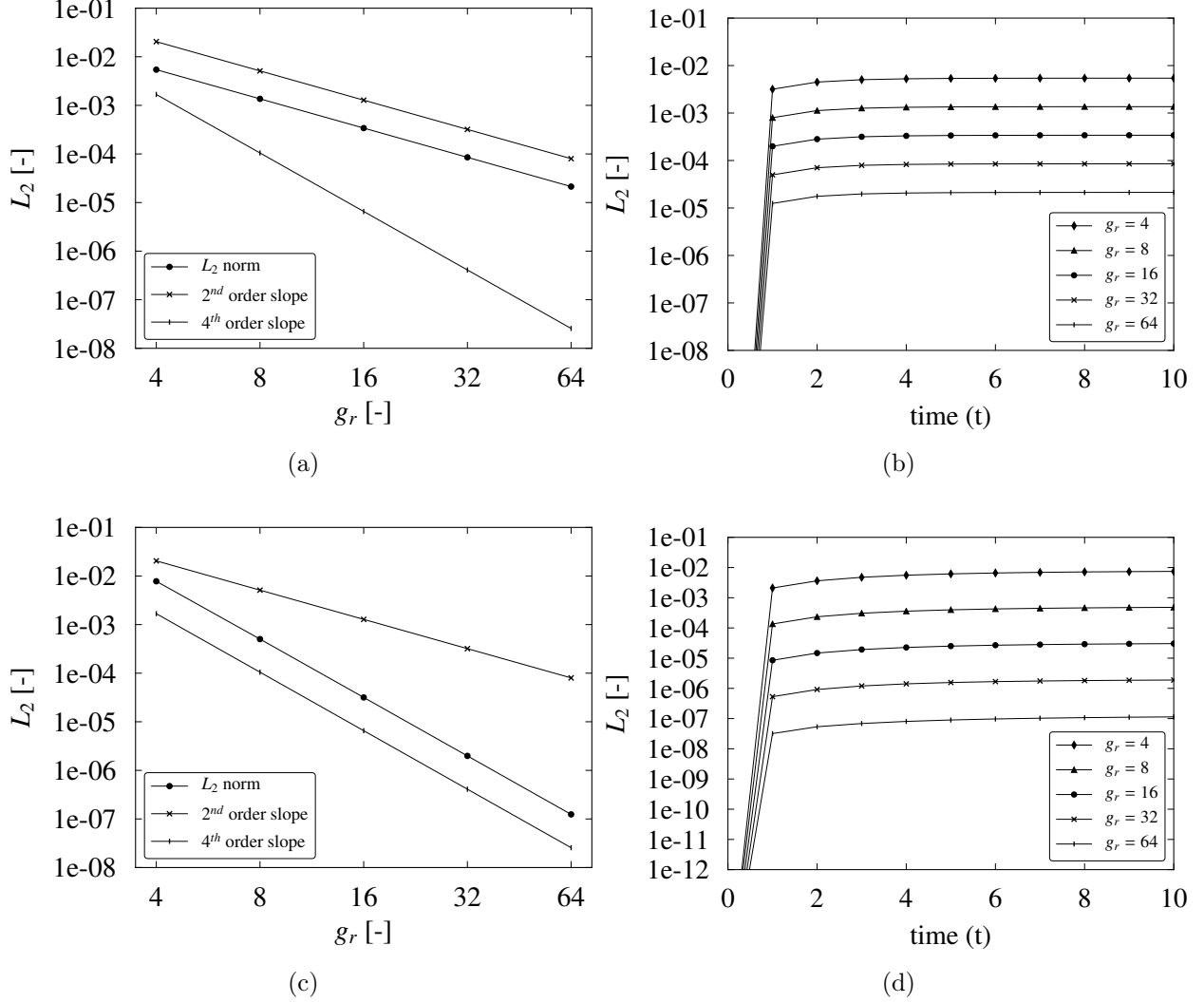


Figure 4: The observed order of accuracy of the code using Eq. 26 for both cases shown in Tab. 4. In first case, the L_2 norm is parallel to the (a) second-order slope and in the second case it is parallel to the (c) fourth-order slope. The resulting curves for the L_2 norm evolution in time are shown for the (b) first and (d) second case. Both L_2 norm evolutions start from values close to the machine precision (10^{-16}), since we start the convergence analysis simulations from the exact solution. In the first case the formal order of accuracy is achieved, $p \approx 2.0$, while in the second case $p^* \approx 4.0$ due to discretization error canceling.

A truncation error canceling could be seen when the choice for the manufactured solution wavenumber was $q_1 = \sqrt{2}q_0$. The latter modifies the expected convergence rate up to fourth-order, which is consistent with the analytical development of the manufactured solution in Eq. 23. To verify the general case, we construct a manufactured solution with $q_1 \neq \sqrt{2}q_0$. Following this approach, a second-order convergence rate is recovered as theoretically expected.

The numerical scheme has been proven to be consistent, unconditionally stable and truly second-order accurate in space, in the general case. The chosen grid resolution for the numerical experiments, presented in the next section, was $g_r = 16$, which has a good trade-off between resolution and computational cost in order to represent periodic solutions.

3.3. Lyapunov functional decay

The decay of the “free energy” (Lyapunov) functional is monitored so that we can confirm it is always monotonically decreasing until a minimum value is reached in the steady state. In order to take into account the assumed boundary conditions adopted in this work, we expand the bulk integrals to show that boundary integrals vanish, leading to a new expression for the free energy functional, which is going to be discretized. Using integration by parts and the 2D Gauss theorem (first Green identity), we have:

$$\int_{\Omega} d\mathbf{x} (\psi \nabla^2 \psi) = \oint_{\partial\Omega} \psi \frac{\partial \psi}{\partial n} dl - \int_{\Omega} d\mathbf{x} (\nabla \psi)^2, \quad (27)$$

where the first integral from RHS vanishes for the assumed GDBC, above mentioned. Now Eq. 1 can be rewritten as:

$$\mathcal{F}[\psi] = \int_{\Omega} d\mathbf{x} \frac{1}{2} \left\{ -\epsilon(\mathbf{x}) \psi^2 + \alpha [q_0^4 \psi^2 - 2q_0^2 (\nabla \psi)^2 + (\nabla^2 \psi)^2] - \frac{\beta}{2} \psi^4 + \frac{\gamma}{3} \psi^6 \right\}. \quad (28)$$

The Lyapunov functional associated to the SH equation is implemented through the discrete formula derived by Christov & Pontes (2001)[29] for the cubic version, and now extended for the quintic one. The formula presents a $\mathcal{O}(\Delta t^2 + \Delta x^2 + \Delta y^2)$ approximation of the functional given by Eq. 2. As pointed by those authors, the monotonic decay of the finite differences version is enforced, provided that the internal iterations converge.

The decay is monitored by:

$$\begin{aligned} \frac{\mathcal{F}^{n+1} - \mathcal{F}^n}{\Delta t} &= - \sum_{i=1}^{n_x} \sum_{j=1}^{n_y} \left(\frac{\psi_{i,j}^{n+1} - \psi_{i,j}^n}{\Delta t} \right)^2 \\ \mathcal{F}^n &= \sum_{i=1}^{n_x} \sum_{j=1}^{n_y} \left[-\frac{\epsilon}{2} (\psi_{i,j}^n)^2 - \frac{\beta}{4} (\psi_{i,j}^n)^4 + \frac{\gamma}{6} (\psi_{i,j}^n)^6 + \frac{\alpha q_0^4}{2} (\psi_{i,j}^n)^2 \right] \\ &\quad - \frac{2\alpha q_0^2}{4} \sum_{i=1}^{n_x} \sum_{j=1}^{n_y} \left[\left(\frac{\psi_{i+1,j}^n - \psi_{i,j}^n}{\Delta x} \right)^2 + \left(\frac{\psi_{i,j}^n - \psi_{i-1,j}^n}{\Delta x} \right)^2 + \left(\frac{\psi_{i,j+1}^n - \psi_{i,j}^n}{\Delta y} \right)^2 + \left(\frac{\psi_{i,j}^n - \psi_{i,j-1}^n}{\Delta y} \right)^2 \right] \\ &\quad + \frac{\alpha}{2} \sum_{i=1}^{n_x} h^{n_x} \sum_{j=1}^{n_y} \left[\frac{\psi_{i+1,j}^n - 2\psi_{i,j}^n + \psi_{i-1,j}^n}{\Delta x^2} + \frac{\psi_{i,j+1}^n - 2\psi_{i,j}^n + \psi_{i,j-1}^n}{\Delta y^2} \right]^2 \end{aligned} \quad (29)$$

In order to check if the Lyapunov functional is correctly implemented, we ran two simulations with the cubic SH (with ramped ϵ) and four with the quintic one (both uniformly and ramped ϵ), and monitored the evolution of the functional, of \dot{L}_1 and of the patterns observed through the order parameter $\psi(\mathbf{x}, t)$. The patterns evolution and the associated \dot{L}_1 and Lyapunov potentials are presented in Figs. 5, 7, and 8. The simulations were run with ramps of the control parameter $\epsilon(\mathbf{x})$ along the x -direction for both GDBC and PBC. The two simulations with the SH3 model started from the same pseudo-random initial condition. The four simulations with the SH35 model started from a squared localized patch in the center of the cell. This pre-existing structure of stripes parallel to the y -direction were constructed by:

$$\psi(\mathbf{x}, 0) = A_0 \cos(q_0 x), \quad (30)$$

where $A_0 = \left\{ (\beta/(2\gamma)) [1 + \sqrt{1 + \epsilon\gamma/\beta^2}] \right\}^{1/2}$, which is compatible with the expected field ψ amplitude for a stable spatially homogeneous states, for the SH35 [12]. The results of these six simulations confirm the correct implementation of the Lyapunov functional for both equations, with a monotonic decay in all cases.

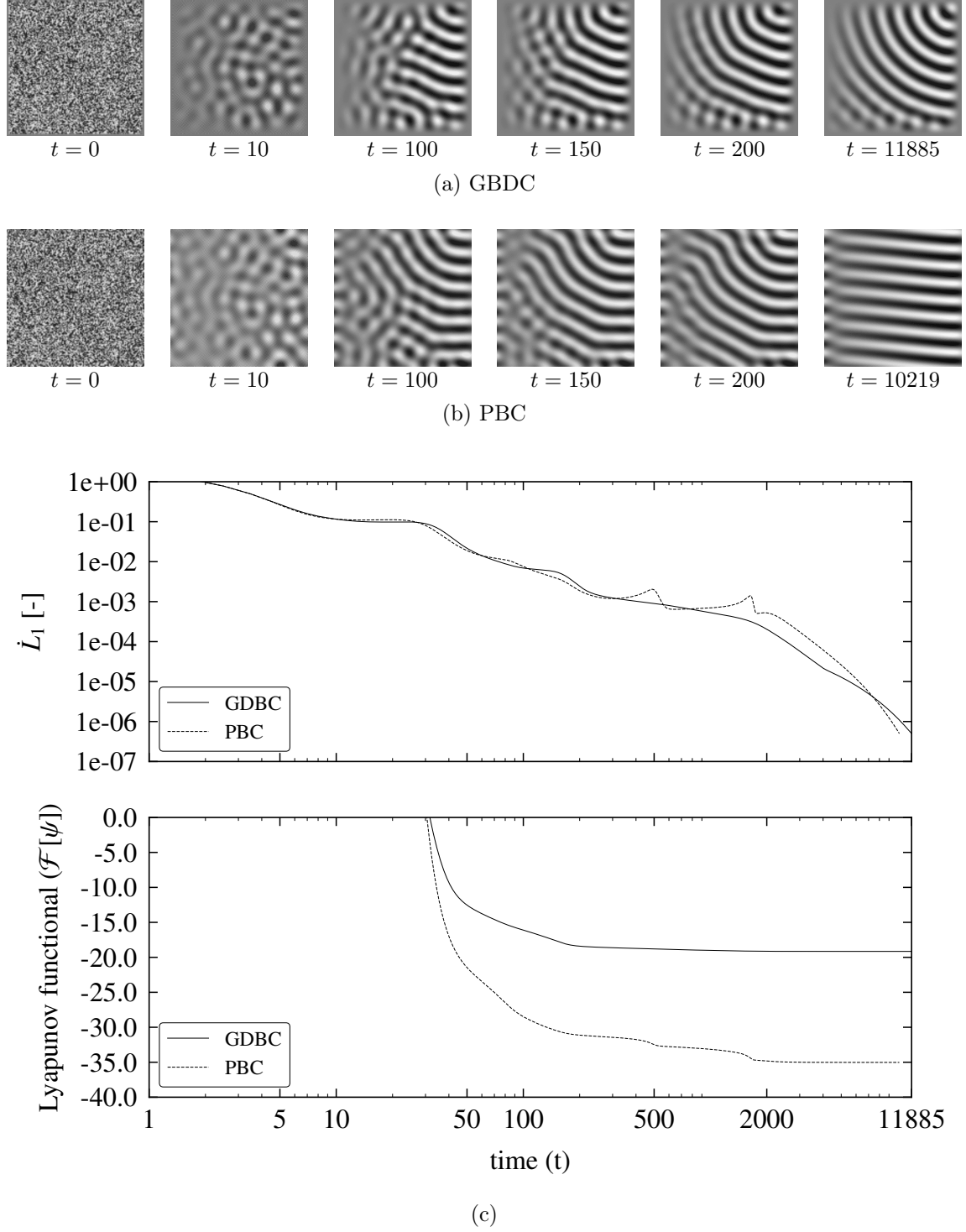
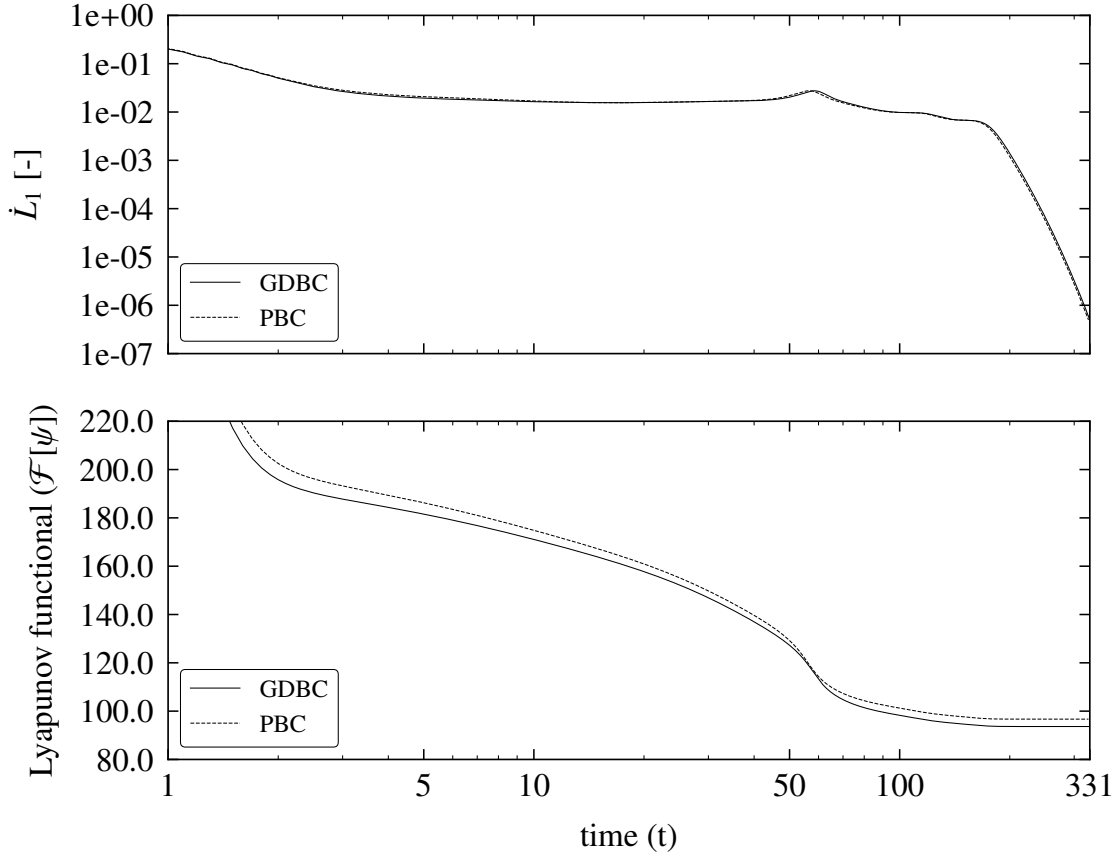
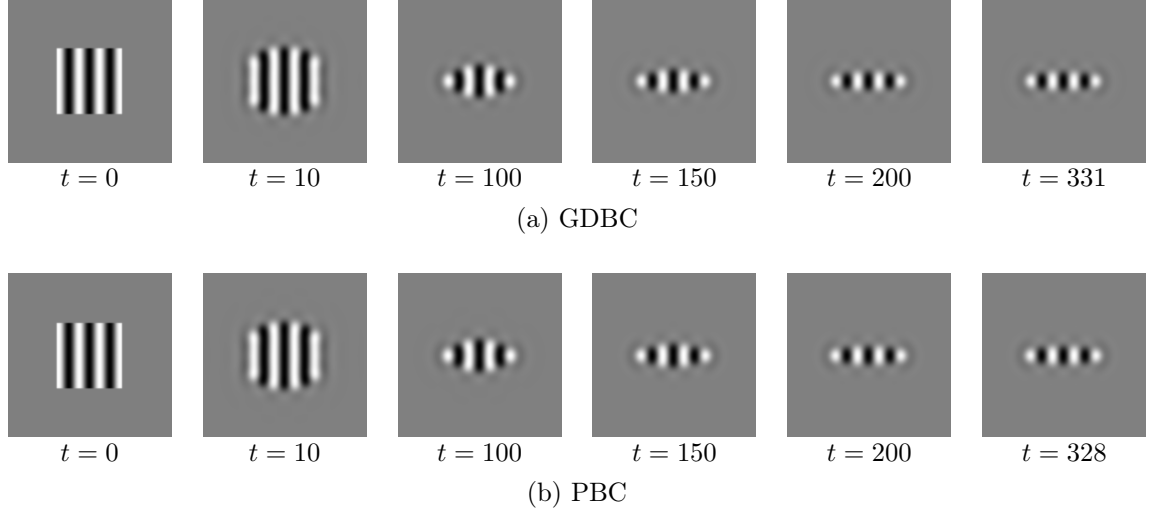


Figure 5: The results of two simulations run to verify the correctness of the implementation of the Lyapunov functional for the SH3 model. First and second rows: SH3 pattern evolution for a ramped system forced with $0.0 \leq \epsilon \leq 0.2$ GDBC (a) and PBC (b), respectively, until the indicated steady state.. Both simulations started with the same pseudo-random initial condition. \dot{L}_1 and the Lyapunov potential evolutions are showed below.



(c)

Figure 6: The results of two simulations run to verify the correctness of the implementation of the Lyapunov functional for the SH35 model. First and second rows: SH35 pattern evolution for a uniformly forced system with $\epsilon = -1.5$, GDBC (a) and PBC (b), respectively, until the indicated steady state.. Both simulations started from the same pre-existing structure of rolls perpendicular to the gradient of the control parameter. \dot{L}_1 and the Lyapunov potential evolutions are showed below.

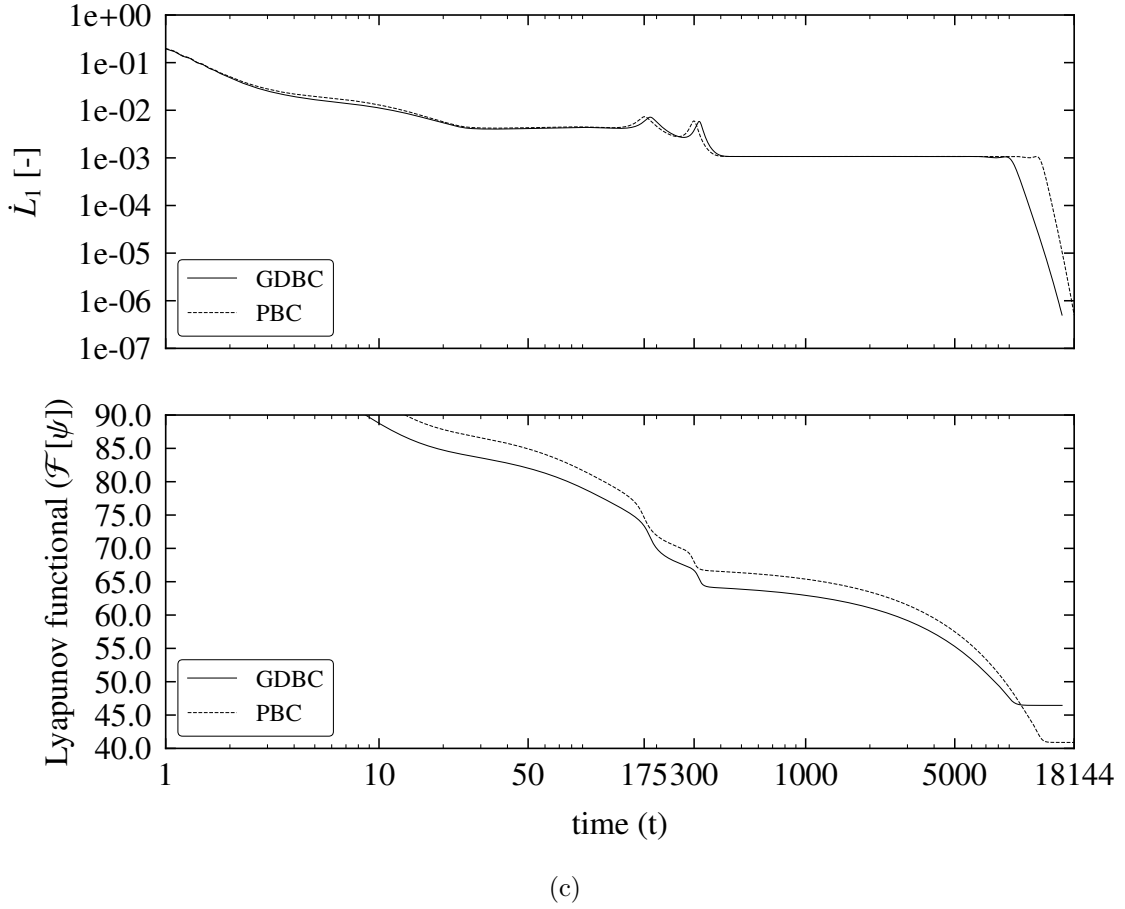
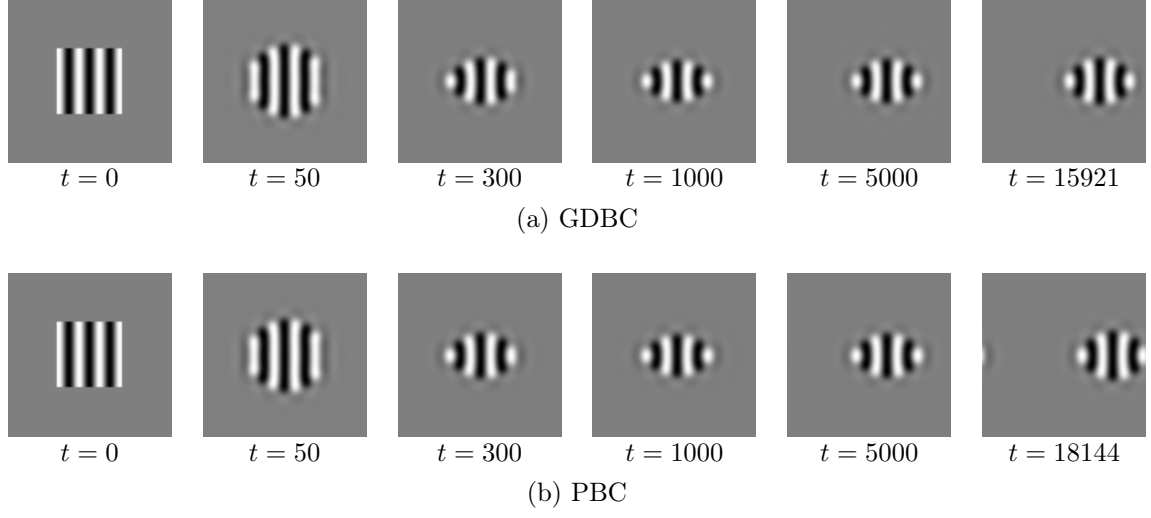
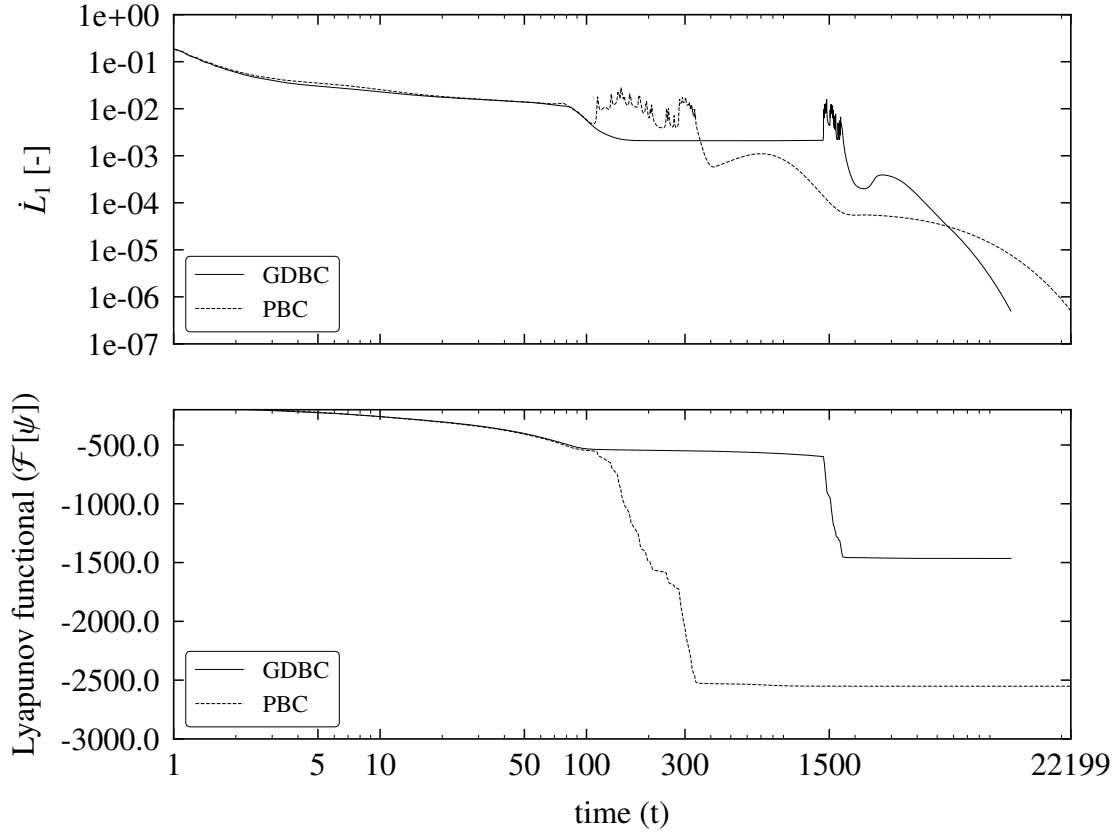
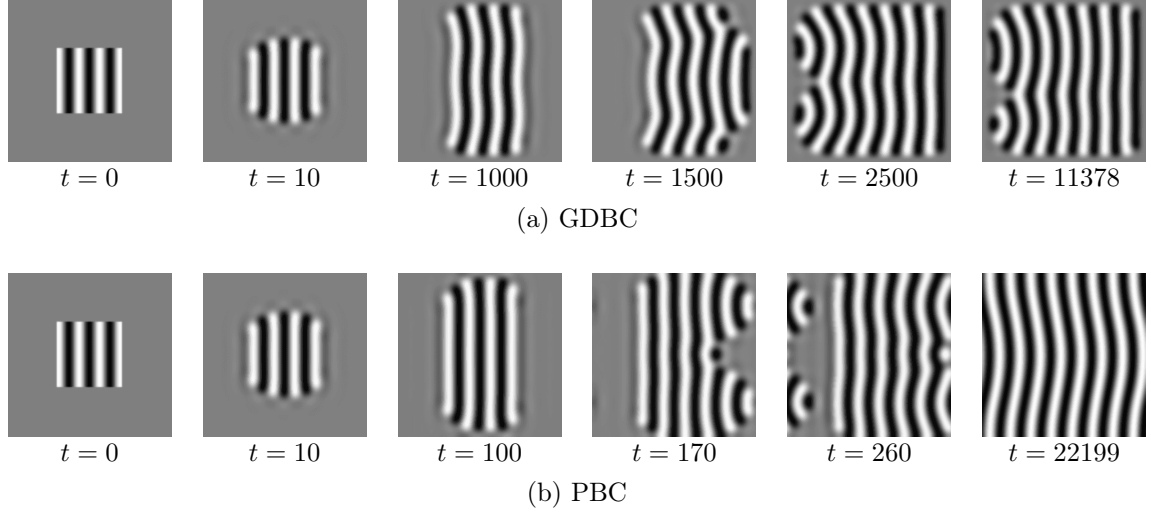


Figure 7: The results of two simulations run to verify the correctness of the implementation of the Lyapunov functional for the SH35 model. First and second rows: SH35 pattern evolution for a ramped system forced with $-1.5 \leq \epsilon \leq -1.4$, GDBC (a) and PBC (b), respectively, until the indicated steady state.. Both simulations started from the same pre-existing structure of rolls perpendicular to the gradient of the control parameter. \dot{L}_1 and the Lyapunov potential evolutions are showed below.



(c)

Figure 8: The results of two simulations run to verify the correctness of the implementation of the Lyapunov functional for the SH35 model. First and second rows: SH35 pattern evolution for a ramped system forced with $-1.4 \leq \epsilon \leq -1.2$, GDBC (a) and PBC (b), respectively, until the indicated steady state.. Both simulations started from the same pre-existing structure of rolls perpendicular to the gradient of the control parameter. \dot{L}_1 and the Lyapunov potential evolutions are showed below.

4. Numerical experiments

The numerical scheme described in Sec. 2 was used to solve the SH3 and the SH35 equations in square domains with rigid and periodic boundary conditions, and with nonuniform forcings. The parameter values adopted are given in Tabs. 1, 5 and 6. All simulations were done in a satisfactory grid resolution of the spatial grid of 16 points per critical wavelength ($g_r = 16$).

4.1. Numerical experiments with the SH3 equation

In the case of the SH3 equation we present the result of ten simulations (denoted as configurations 1 to 10), five of them with GDBC and five with PBC. The resulting steady state for each simulation are summarized in Fig. 9. All simulations started with the same pseudo-random initial condition. For each type of boundary condition we ran a configuration with uniform forcing to reproduce existing results, two configurations with ramps of the control parameter ϵ , as detailed in Tab. 5, and two ones with different gaussian distributions of the control parameter. In ramped systems, the parameter is assumed as uniform along the y -direction. The gaussian distribution of ϵ introduces symmetric gradients in the radial direction.

The steady state solutions obtained are shown in Fig. 9. The first line in this figure shows the distribution of the control parameter ϵ along the x -direction of the domain. Second and fourth lines present the steady state solutions with rigid and with periodic boundary conditions, respectively. Third and fifth lines present the same results shown in lines two and four, but this time with frames constructed with enhanced contrast to make visible the subcritical structure developed in regions where the control parameter ϵ is negative. Each configuration run is identified with an assigned number.

Configuration 1 shows a pattern emerging in a uniformly forced system with GDBC, in qualitative agreement with previous results [22, 25, 26, 28]. The case was run in the verification framework our numerical code. A pattern with unavoidable defects is developed, in order to match the strong requirement of rolls approaching perpendicularly the side walls. A structure with lower density of defects appears in configuration 6, where the same forcing of Frames 1 is assumed, but now, with periodic boundary conditions. The pattern develops a zig-zag instability.

Configuration 2 reproduces the result of a pattern developed in presence of a ramped control parameter ϵ , with a subcritical region [27, 29, 28]. A structure with smaller amount of defects emerges, thanks to the fact that the weak structure of rolls parallel to the wall appears in the subcritical region. A similar situation occurs in configuration 3, where the system is forced with a ramp of the control parameter ϵ , however taking non negative values. In this case a weak structure of rolls perpendicular to the lower ($y = 0$) sidewall is visible.

Configurations 7 and 8 present the results for systems with same forcing of configurations 2 and 3, but with periodic boundary conditions. A tendency to develop a structure of rolls parallel to the gradient of the control parameter ϵ clearly appears, as well as the existence of a Benjamin-Feir instability close to the left wall, induced by the the supercritical region close to the right wall.

Table 5: Parameters assumed for the numerical experiments with the SH3 equation.

Parameter	Formulae	Value	Description
q_0	-	1.0	Critical wavenumber
λ_0	$2\pi/q_0$	2π	Critical wavelength
w_x, w_y	-	10	Wavelengths per domain length
g_r	-	16	Grid resolution (nodes per wavelength)
n_x, n_y	$w_x \times g_r, w_y \times g_r$	160	Nodes per mesh side (n)
N	$n_x \times n_y$	160×160	Total number of mesh nodes
L_x, L_y	$w_x \lambda_0, w_y \lambda_0$	≈ 62.832	Square domain length (L)
$\Delta x, \Delta y$	$L/(n-2)$	≈ 0.3977	Space step (GDBC)
$\Delta x, \Delta y$	L/n	≈ 0.3927	Space step (PBC)
Δt	-	0.5	Time step for SH3
A	-	0.2	Gaussian maximum value (peak)
R_1	N	-	For configurations 4 and 9
R_2	$0.2N$	-	For configurations 5 and 10
x_0, y_0	$L_x/2, L_y/2$	-	Gaussian center

Configurations 4, 5, 9 and 10 present the result of simulations performed with a Gaussian radial distribution of the control parameter ϵ , in the form:

$$\epsilon(\mathbf{x}) = Ae^{-R((x-x_0)^2+(y-y_0)^2)}, \quad (31)$$

where the parameters are specified in Tab. 5. The parameter R is assumed to be R_1 in configurations 4 and 9; and R_2 in configurations 5 and 10. Worth noticing that these gaussian distributions introduce a gradient of ϵ in all directions with the maximum of ϵ at the center of the domain.

Configurations 4 and 5 were run with rigid boundary conditions and configurations 9 and 10, with periodic conditions. A sharp Gaussian, rapidly decreasing from the maximum value across a short distance, leads to the onset of a target pattern with both boundary conditions. The target pattern collapses in presence of a wider Gaussian distribution of the control parameter ϵ , leading to a structure of rolls. The structure wavevector takes the direction of one of the domain diagonals, again, since the most difficult direction for modulations of the structure is the one associated to the wavevector, whereas the easiest one is the direction perpendicular to the wavevector.

The time evolution of configurations 3 (GDBC) and 8 (PBC), from the pseudo-random initial condition to the steady state is shown in Fig. 10. The evolution of configurations 5 (GDBC) and 10 (PBC) are shown in Fig. 11. All curves show the expected result, with \dot{L}_1 rapidly decreasing as a pattern emerges and the

amplitude of the structure essentially saturates. This stage is followed by a much slower phase dynamics, ending with an exponential decay towards the steady state. In general, \dot{L}_1 peaks are associated to the removal of defects. We observe that boundary conditions have little effect on the resulting curves.

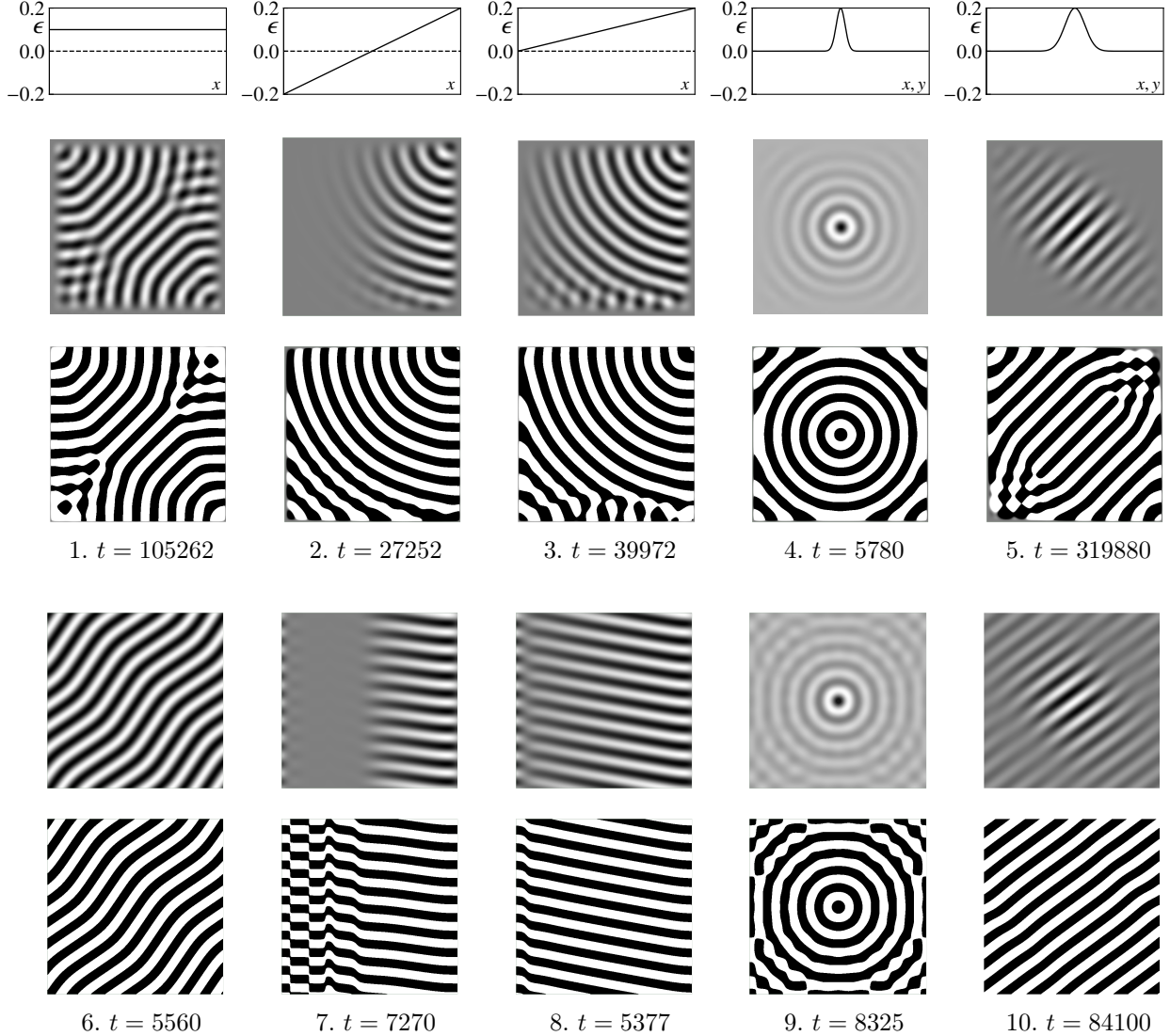
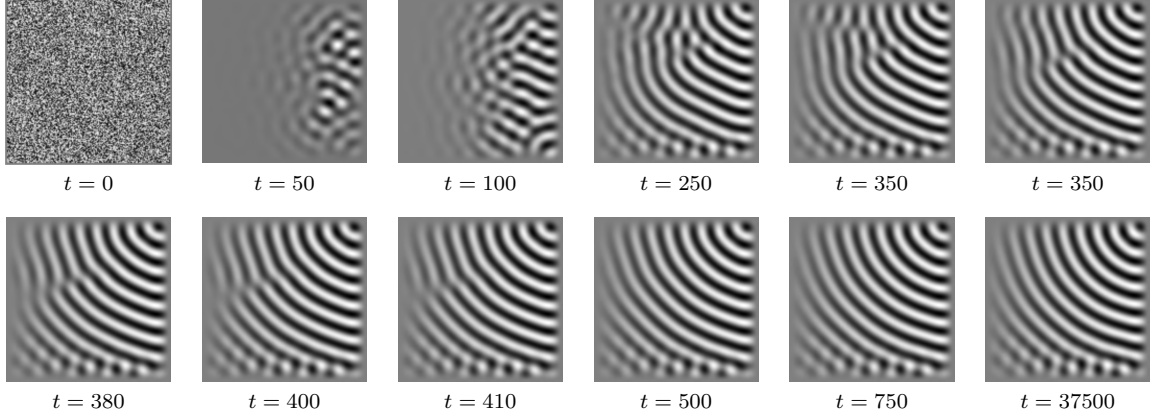
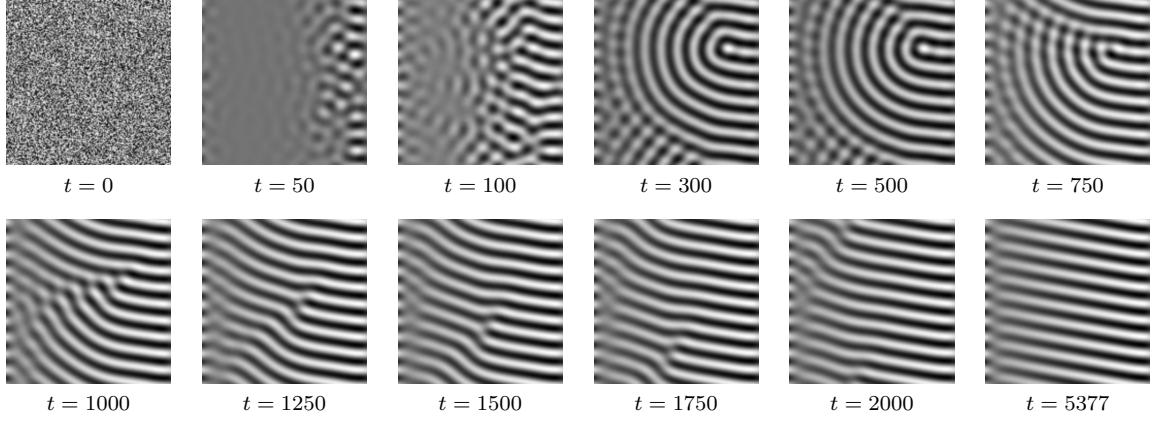


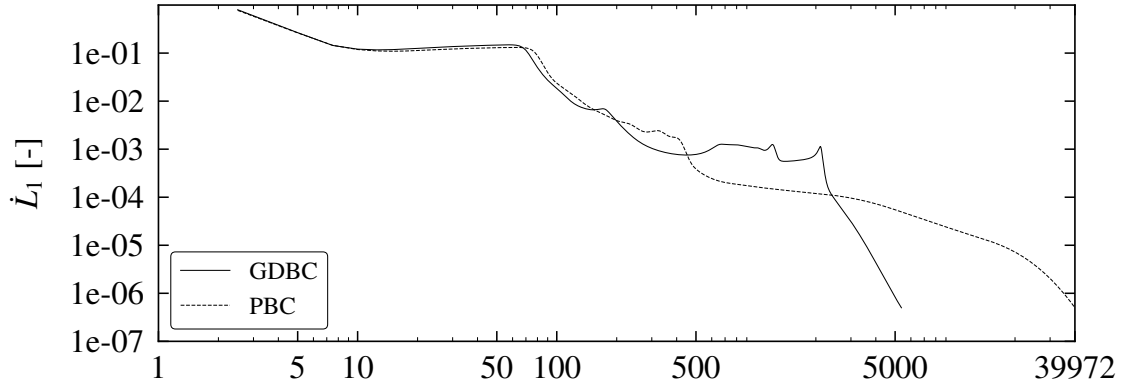
Figure 9: Zoology of ten patterns obtained by numerical integration of the SH3 equation with GDBC (rows 1 and 2) and PBC (rows 3 and 4). All patterns shown correspond to the steady attained when $\dot{L}_1 \leq 5.0 \times 10^{-7}$ (Eq. 21). All simulations started from the same pseudo-random initial condition. The applied forcing is shown in the first row. First column: uniform forcing; Second and third columns: ramps of the control parameter ϵ ; Fifth and sixth columns: Two Gaussian forcings, according to Eq.31. The first and third rows correspond to GDBC and PBC, respectively. Second and fourth rows contains the same patterns shown in rows one and three, respectively, with an enhanced contrast. Patterns configurations 2 and 3 tend to approach perpendicularly to the supercritical boundaries and parallel to subcritical ones. The pattern configuration 4 presents a target structure compatible with the narrow Gaussian profile of the forcing. The target collapses in the pattern configuration 5, and evolves to a structure of rolls parallel to one of diagonals, and not to the side walls. This effect occurs as a consequence of the modulation, which is harder along the direction of the pattern wavevector. Similar phenomena occurs with patterns configurations 9 and 10.



(a) GDBC



(b) PBC



(c)

Figure 10: First and second lines: pattern evolution for the configuration 3 of Fig. 9, with GDBC (a), until the steady state. Third and fourth lines: pattern evolution for the configuration 8 of Fig. 9, with PBC (b), until the steady state. In both cases, the system is forced with a ramp of the control parameter ϵ along the x direction, with $-0.2 \leq \epsilon \leq 0.2$. The associated $\dot{L}_1 \times t$ curves are also shown (c).

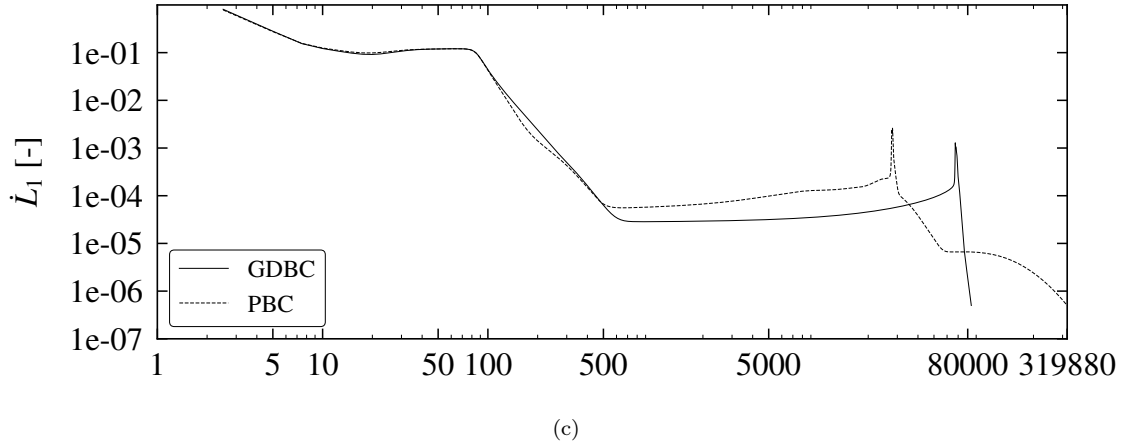
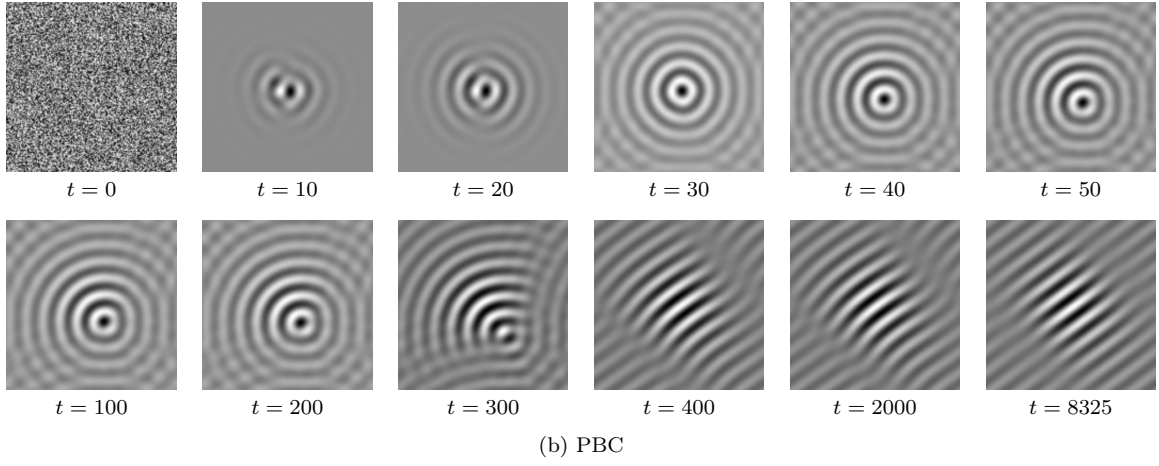
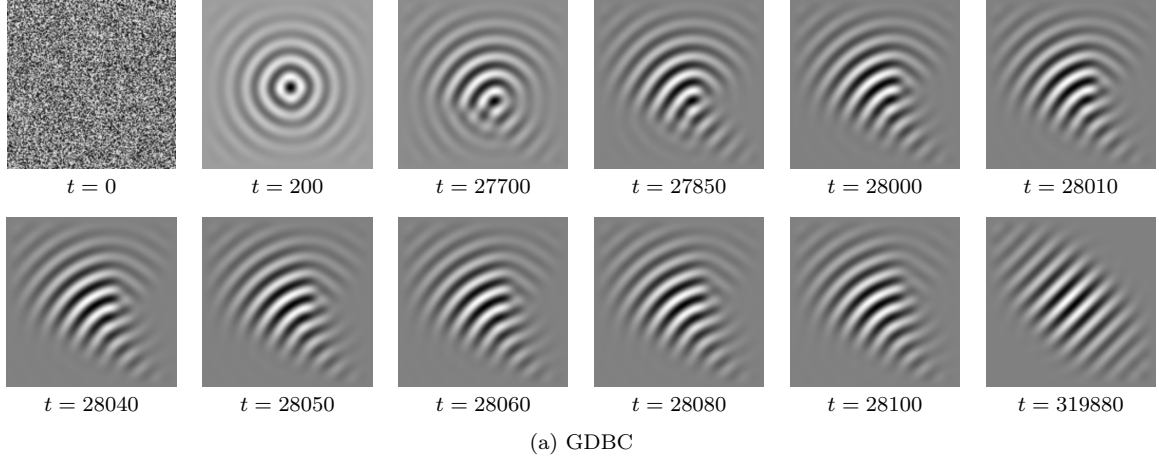


Figure 11: First and second lines: pattern evolution for the configuration 5 of Fig. 9, with GDBC (a), until the steady state. Third and fourth lines: pattern evolution for the configuration 10 of Fig. 9, with PBC (b), until the steady state. In both cases, the system is forced with a gaussian distribution of the control parameter ϵ . The associated $\dot{L}_1 \times t$ curves are also shown (c).

4.2. Numerical experiments with the SH35 equation

The quintic version of the Swift-Hohenberg equation with destabilizing cubic term allows for the existence of stable localized solutions for an interval of subcritical values of ϵ , i.e. coexistence of the solution $\psi = 0$ and a modulated one, shown by [12]. The parameter values adopted are given in Tab.6. In this sense, we run six experiments with the SH35 equation: two with uniform forcing ($\epsilon = -1.5$), GDBC and PBC, respectively, two with a ramp $-1.5 \leq \epsilon \leq -1.4$, GDBC and PBC, respectively, and two last ones with a ramp $-1.4 \leq \epsilon \leq -1.2$, GDBC and PBC, respectively. The experiments with uniform forcing were conducted as code verification, to reproduce existing results. The time evolution of these two experiments are shown in Fig. 6. Both simulations started from the same pseudo-random initial condition.

The four experiments with ramped systems started from the same pre-existing structure of rolls perpendicular to the gradient of the control parameter. These experiments were used to verify the implementation of the Lyapunov functional with the quintic equation SH35. The evolution of these simulations are shown in Fig. 7, and 8. In the case of a ramp given by $-1.5 \leq \epsilon \leq -1.4$ the pre-existing structure evolves towards a localized structure of rolls with the same orientation of the initial condition, with both boundary conditions. When the applied forcing takes the form $-1.4 \leq \epsilon \leq -1.2$, lowering the energy associated with the non-trivial solution both with GDBC and PBC, a structure of rolls with the same orientation of the initial condition also prevails, but the final structure is localized with GDBC and occupies the entire domain, with PBC.

Table 6: Parameters assumed for the numerical experiments with the SH35 equation.

Parameter	Formulae	Value	Description
q_0	-	1.0	Critical wavenumber
λ_0	$2\pi/q_0$	2π	Critical wavelength
w_x, w_y	-	8	Wavelengths per domain length
g_r	-	16	Grid resolution (nodes per wavelength)
n_x, n_y	$w_x \times g_r, w_y \times g_r$	128	Nodes per mesh side (n)
N	$n_x \times n_y$	128×128	Total number of mesh nodes
L_x, L_y	$w_x \lambda_0, w_y \lambda_0$	≈ 50.266	Square domain length (L)
$\Delta x, \Delta y$	$L/(n-2)$	≈ 0.3989	Space step (GDBC)
$\Delta x, \Delta y$	L/n	≈ 0.3927	Space step (PBC)
Δt	-	0.1	Time step for SH35

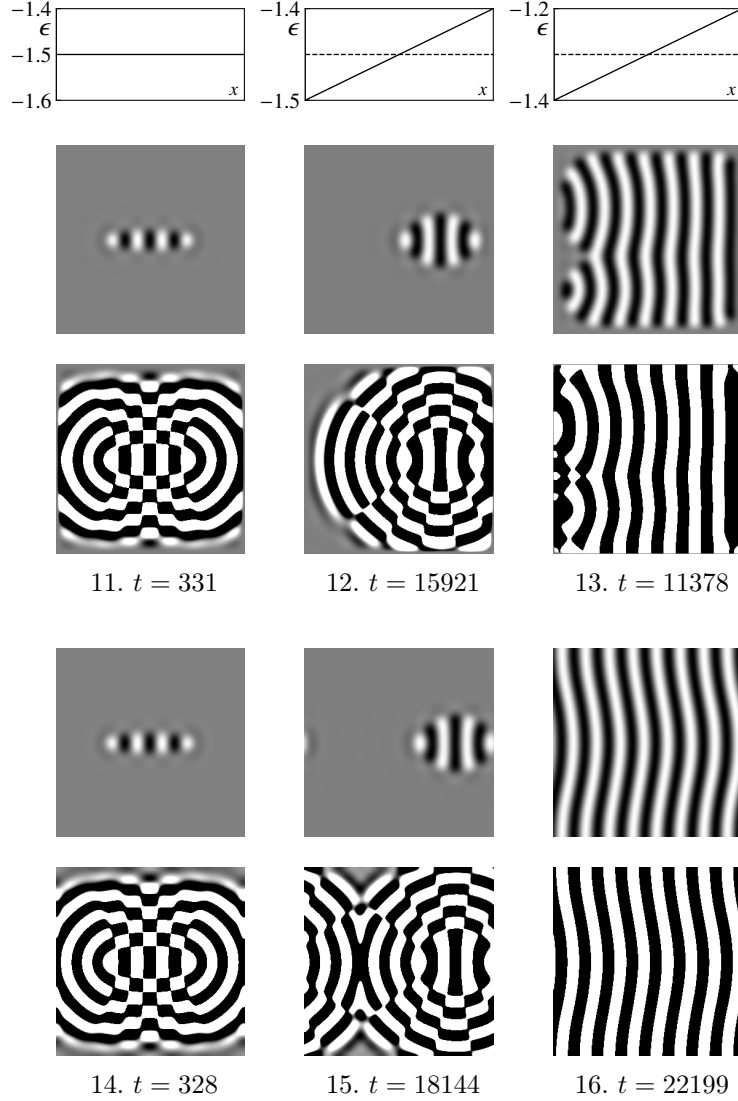


Figure 12: Zoology of six patterns obtained by numerical integration of the SH35 equation with GDBC (rows 1 and 2) and PBC (rows 3 and 4). All patterns shown correspond to the steady attained when $\dot{L}_1 \leq 5.0 \times 10^{-7}$ (Eq. 21). All simulations started from a pre-existing structure of stripes oriented along the y direction. The applied forcing is shown in the first row. First column: uniform forcing with $\epsilon = -1.5$. Second column: forcing with ramp of the control parameter in the form $-1.5 \leq \epsilon \leq -1.4$. Third column: ramp in the form $-1.4 \leq \epsilon \leq -1.2$. The first and third rows correspond to GDBC and PBC, respectively. Second and fourth rows contain the same patterns shown in rows one and three, respectively, with an enhanced contrast. In all cases, the pre-existing structure of stripes oriented along the y prevails at the steady state. However, configurations 11, 12, 14 and 15 evolved to localized structures, whereas, in the case of configurations 13 and 16 the resulting pattern occupy the entire domain.

4.3. Discussion

In the present endeavor, we extended a numerical scheme proposed by Christov & Pontes [28] to investigate pattern formation modelled by the cubic Swift-Hohenberg equation in two dimensions. The original scheme presents second order representation of all derivatives, strict implementation of the associated Lyapunov functional, rigid boundary conditions (GDBC), and a semi-implicit time discretization of the terms, aiming

at constructing negative definite operators that assure the unconditional stability of the scheme.

The present work includes the quintic version of the Swift-Hohenberg equation and PBC for both the cubic and the quintic versions of the model. The scheme retains all characteristics of the original one, namely strict representation of the Lyapunov functional, unconditional stability, and second order representation of all derivatives. In addition, we also included a convergence analysis of the scheme, verification tests, and an initial evaluation of the effect of nonuniform forcings in the resulting pattern. The nonuniform forcings adopted in the present work consist of spatial ramps and of gaussian distributions of the control parameter ϵ . A detailed study of the effects of nonuniform forcings will be addressed in a forthcoming paper.

Verification tests consisted in qualitatively reproducing existing results of simulations with the SH3 and SH35 equations with uniform forcings and both GDBC and PBC. Good agreement was achieved. As an additional verification procedure, we also found good agreement between the results with the SH3 forced with a spatial ramp of ϵ , and those presented by Pontes *et al.* (2008)[28]. In that work, the authors adopted GDBC and a first order in time scheme. The results of the SH3 equation with GDBC and ramps of ϵ are presented in Figs. 2, 5a and in simulations configurations 1, 2 and 3 of Fig. 12.

Rigid boundary conditions (GDBC) make patterns of supercritical stripes developed close to different boundaries to compete, due to the tendency of stripes to approach boundaries perpendicularly to them. Stripes cannot be perpendicular to all boundaries simultaneously. In addition, boundary effects compete with bulk ones. The overall result is a structures with high density of defects. A different situation occurs when PBC are imposed. In this case, a periodicity is imposed to the emerging pattern, and boundary effects are excluded. The result is, in general, a pattern with fewer defects than ones developed with the same forcing and GDBC. This is also the case when the system is forced with nonuniform distributions of the control parameter.

An important configuration in nonuniformly forced systems consists in adopting GDBC, and a forcing where part of the domain is maintained at subcritical conditions. In this case a less known result points to the fact that the subcritical pattern of stripes, induced by the supercritical region, approach sidewalls parallel to them. These patterns are automatically perpendicular to adjacent walls. As a result, nonuniformly forced systems with a subcritical region tend to develop patterns with a lower density of defects than systems uniformly forced [28]. The presented simulations reproduce this effect.

A particular feature observed in nonuniformly forced systems, using the SH3 equation, PBC and spatial ramps of the control parameter, consists in the development of several examples of the Benjamin-Feir instability, which manifest itself in the form of “alternating” rolls, in a dislocation sense, promoted by a region where minimum and maximum values of ϵ are close.

The quintic SH35 equation with a destabilizing cubic term allows for the emergence of localized solutions in an interval of subcritical values of ϵ . Six simulations were run with the quintic equation, assuming three different forcings and two boundary conditions for each one. All simulations started from the same pseudo-random initial condition. The resulting steady states are presented in Fig. 12. The first group consisted

of two simulations with uniform forcing $\epsilon = -1.5$. These simulations are denoted by configurations 11 and 14 in Fig. 12. The second group was forced with a ramp along the x direction, given by $-0.2 \leq \epsilon \leq 0.2$ (configurations 12 and 15). The third group was run with $0.0 \leq \epsilon \leq 0.2$ (configurations 13 and 16). In all configurations, the resulting patterns consisted of stripes perpendicular to the gradient of the control parameter, with localized patterns in the first and second groups, and the stripes occupying the entire domain in the third group.

A mesh of $g_r = 16$ points per critical wavelength was adopted in all simulations, which represents a good trade-off between spatial resolution and computational cost.

5. Conclusion

In this article, we extended a numerical scheme proposed by Christov & Pontes [28] to investigate pattern formation modeled by the cubic Swift-Hohenberg equation SH3 in two dimensions. The original scheme presents second order representation of all derivatives, strict implementation of the associated Lyapunov functional, rigid boundary conditions (GDBC), and a semi-implicit assignment of the terms.

The present work includes the quintic version of the Swift-Hohenberg equation and periodic boundary conditions (PBC) for both the cubic and the quintic versions of the model. The scheme retains all characteristics of the original one, namely strict representation of the Lyapunov functional, unconditional stability, and second order representation of all derivatives. In addition, we also included a convergence analysis, new verification tests, and an initial evaluation of the effect of nonuniform forcings in the form of spatial ramps and of gaussian distributions of the control parameter ϵ . Among the verification tests, the convergence analysis confirmed the truly second-order accuracy of the scheme both in space and time and the existence of localized structures developed in the framework of the SH35 equation even with nonuniform forcings. The numerical experiments conducted in this work suggest the existence of effects and the onset of patterns not addressed in the literature. Both questions will be the object of a forthcoming paper.

The conducted tests confirmed the robustness of the developed tool for pursuing the investigation of the pattern formation through the parabolic Swift-Hohenberg equation presenting various nonlinear terms, including nonuniform forcings.

6. Acknowledgments

The authors thank FAPERJ (Research Support Foundation of the State of Rio de Janeiro) and CNPq (National Council for Scientific and Technological Development) for the financial support. Daniel Coelho acknowledges a fellowship from the Coordination for the Improvement of Higher Education Personnel-CAPES (Brazil). A FAPERJ Senior Researcher Fellowship is acknowledged by J. Pontes. The authors dedicate a special posthumous thanks to C. I. Christov, who performed great development regarding the numerical methods addressed in this paper.

References

- [1] L. Yang, A. M. Zhabotinsky, I. R. Epstein, Stable squares and other oscillatory turing patterns in a reaction-diffusion model, *Physical review letters* 92 (2004) 198303.
- [2] J. V. Moloney, A. C. Newell, *Nonlinear Optics*, Westview Press, 2008.
- [3] D. Walgraef, *Spatio-Temporal Pattern Formation: With Examples from Physics, Chemistry, and Materials Science, Partially Ordered Systems*, 1 ed., Springer-Verlag New York, 1997.
- [4] N. Ghoniem, D. Walgraef, *Instabilities and Self-organization in Materials*, Oxford Univ. Press, 2008.
- [5] N. Provatas, K. Elder, *Phase-Field Methods in Materials Science and Engineering*, Wiley, 2010.
- [6] M. Plapp, A. Karma, Multiscale finite-difference-diffusion-monte-carlo method for simulating dendritic solidification, *Journal of Computational Physics* 165 (2000) 592–619.
- [7] N. Provatas, M. Greenwood, B. Athreya, N. Goldenfeld, J. Dantzig, Multiscale modeling of solidification: phase-field methods to adaptive mesh refinement, *International Journal of Modern Physics B* 19 (2005) 4525–4565.
- [8] S. Ghosh, M. Plapp, Influence of interphase boundary anisotropy on bulk eutectic solidification microstructures, *Acta Materialia* 140 (2017) 140–148.
- [9] S. Ghosh, A. Karma, M. Plapp, S. Akamatsu, S. Bottin-Rousseau, G. Faivre, Influence of morphological instability on grain boundary trajectory during directional solidification, *Acta Materialia* 175 (2019) 214–221.
- [10] J. Swift, P. C. Hohenberg, Hydrodynamic fluctuations at the convective instability, *Physical Review A* 15 (1977).
- [11] J. Pontes, D. Walgraef, E. Aifantis, On dislocation patterning: Multiple slip effects in the rate equation approach, *International journal of plasticity* 22 (2006) 1486–1505.
- [12] H. Sakaguchi, H. R. Brand, Stable localized solutions of arbitrary length for the quintic Swift-Hohenberg equation, *Physica D* 97 (1996) 274–285.
- [13] I. Walton, On the onset of Rayleigh-Bénard convection in a fluid layer of slowly increasing depth, *Studies in Applied Mathematics* 67 (1982) 199–216.
- [14] I. Walton, The onset of cellular convection in a shallow two-dimensional container of fluid heated non-uniformly from below, *Journal of Fluid Mechanics* 131 (1983) 455–470.
- [15] K. Elder, M. Katakowski, M. Haataja, M. Grant, Modeling elasticity in crystal growth, *Physical review letters* 88 (2002) 245701.

- [16] K. Elder, M. Grant, Modeling elastic and plastic deformations in nonequilibrium processing using phase field crystals, *Physical Review E* 70 (2004) 051605.
- [17] J. Langer, H. Müller-Krumbhaar, Theory of dendritic growth—i. elements of a stability analysis, *Acta Metallurgica* 26 (1978) 1681–1687.
- [18] J. S. Langer, Instabilities and pattern formation in crystal growth, *Reviews of modern physics* 52 (1980) 1.
- [19] M. Elsey, B. Wirth, A simple and efficient scheme for phase field crystal simulation, *ESAIM: Mathematical Modelling and Numerical Analysis* 47 (2013) 1413–1432.
- [20] H. G. Lee, J. Kim, A simple and efficient finite difference method for the phase-field crystal equation on curved surfaces, *Computer Methods in Applied Mechanics and Engineering* 307 (2016) 32–43.
- [21] Y. Li, J. Kim, An efficient and stable compact fourth-order finite difference scheme for the phase field crystal equation, *Computer Methods in Applied Mechanics and Engineering* 319 (2017) 194–216.
- [22] H. S. Greenside, J. W. M. Coughran, Nonlinear pattern formation near the onset of Rayleigh-Bénard convection, *Physical Review A* 30 (1984) 398–428.
- [23] M. Cross, Ingredients of a theory of convective textures close to onset, *Physical Review A* 25 (1982) 1065.
- [24] M. Cross, Boundary conditions on the envelope function of convective rolls close to onset, *The Physics of Fluids* 25 (1982) 936–941.
- [25] P. Manneville, *Non-equilibrium Structures and Weak Turbulence*, Academic Press: San Diego, CA, USA, 1990.
- [26] M. C. Cross, Pattern formation outside equilibrium, *Rev. Modern Physics* 65 (1983) 851–1112.
- [27] C. Christov, J. Pontes, D. Walgraef, M. Velarde, Implicit time splitting for fourth-order parabolic equations, *Computer Methods in Applied Mechanics and Engineering* 148 (1997).
- [28] J. Pontes, D. Walgraef, C. I. Christov, Pattern formation in spatially ramped Rayleigh-Bénard systems, *Journal of Computational Interdisciplinary Sciences* 1 (2008) 11–32.
- [29] C. Christov, J. Pontes, Numerical scheme for Swift-Hohenberg equation with strict implementation of Lyapunov functional, *Mathematical and Computer Modelling* 35 (2002).
- [30] H. G. Lee, An energy stable method for the swift-hohenberg equation with quadratic-cubic nonlinearity, *Computer Methods in Applied Mechanics and Engineering* 343 (2019) 40–51.

- [31] E. Vitral, P. H. Leo, J. Viñals, Role of gaussian curvature on local equilibrium and dynamics of smectic-isotropic interfaces, *Physical Review E* 100 (2019) 032805.
- [32] J. Wang, S. Zhai, A fast and efficient numerical algorithm for the nonlocal conservative Swift–Hohenberg equation, *Mathematical Problems in Engineering* (2020).
- [33] J. Douglas, H. H. Rachford., On the numerical solution of heat conduction problems in two and three space variables, *Trans. Amer. Math. Soc.* (1956).
- [34] N. N. Yanenko, M. Holt, *The Method of Fractional Steps*, Springer, 1971.
- [35] E. Vitral, D. Walgraef, J. Pontes, G. Anjos, N. Mangiavacchi, Nano-patterning of surfaces by ion sputtering: Numerical study of the anisotropic damped Kuramoto-Sivashinsky equation, *Computational Materials Science* 146 (2018).
- [36] P. J. Roache, Code verification by the method of manufactured solutions, *J. Fluids Eng.* 124 (2002) 4–10.
- [37] C. J. Roy, Review of code and solution verification procedures for computational simulation, *Journal of Computational Physics* 205 (2005) 131–156.
- [38] V. E. Podneks, I. W. Hamley, Landau-Brazovskii theory for the $Ia\bar{3}d$ structure, *Journal of Experimental and Theoretical Physics Letters* 64 (1996) 617–624.
- [39] D. Boyer, J. Viñals, Grain boundary pinning and glassy dynamics in stripe phases, *Physical Review E* 65 (2002).
- [40] U. M. B. Marconi, P. Tarazona, Dynamic density functional theory of fluids, *Journal of Physics: Condensed Matter* 12 (2000) A413.